

1 **Beijing Climate Center Earth System Model version 1 (BCC-ESM1):**
2 **Model Description and Evaluation of Aerosol Simulations**

3

4 **Tongwen Wu^{1*}, Fang Zhang¹, Jie Zhang¹, Weihua Jie¹, Yanwu Zhang¹, Fanghua Wu¹,**
5 **Laurent Li^{1,2}, Jinghui Yan¹, Xiaohong Liu³, Xiao Lu⁴, Haiyue Tan⁴, Lin Zhang⁴,**
6 **Jun Wang⁵, Aixue Hu⁶**

7

8 ¹Beijing Climate Center, China Meteorological Administration, Beijing, China

9 ²Laboratoire de M é t é o r o l o g i e D y n a m i q u e, I P S L, C N R S, S o r b o n n e U n i v e r s i t é E c o l e N o r m a l e
10 S u p é r i e u r e, E c o l e P o l y t e c h n i q u e, P a r i s, F r a n c e

11 ³ Texas A&M University, College Station, TX, USA

12 ⁴ Laboratory for Climate and Ocean-Atmosphere Studies, Department of Atmospheric and
13 Oceanic Sciences, School of Physics, Peking University, Beijing, China

14 ⁵ University of Iowa, Iowa City, IA 52242, USA

15 ⁶ National Center for Atmospheric Research, PO Box 3000, Boulder, Colorado 80307-3000,
16 USA

17

18

19

20 *Correspondence to:* Tongwen Wu (twwu@cma.gov.cn)

21

22 Submit to Geosci. Model Dev.

23

24 **Revised on Oct. 23, 2019**

25 **Revised on Dec. 14, 2019**

26 **Revised on Jan. 17, 2020**

27 **Revised on Jan. 31, 2020**

28

29 **Abstract.** BCC-ESM1 is the first version of a fully-coupled Earth System Model with
30 interactive atmospheric chemistry and aerosols developed by the Beijing Climate Center,
31 China Meteorological Administration. Major aerosol species (including sulfate, organic
32 carbon, black carbon, dust and sea salt) and greenhouse gases are interactively simulated with
33 a whole panoply of processes controlling emission, transport, gas-phase chemical reactions,
34 secondary aerosol formation, gravitational settling, dry deposition, and wet scavenging by
35 clouds and precipitation. Effects of aerosols on radiation, cloud, and precipitation are fully
36 treated. The performance of BCC-ESM1 in simulating aerosols and their optical properties is
37 comprehensively evaluated as required by the Aerosol Chemistry Model Intercomparison
38 Project (AerChemMIP), covering the preindustrial mean state and time evolution from 1850
39 to 2014. The simulated aerosols from BCC-ESM1 are quite coherent with
40 CMIP5-recommended data, in-situ measurements from surface networks (such as IMPROVE
41 in the U.S. and EMEP in Europe), and aircraft observations. A comparison of modeled
42 aerosol optical depth (AOD) at 550 nm with satellite observations retrieved from Moderate
43 Resolution Imaging Spectroradiometer (MODIS) and Multi-angle Imaging
44 SpectroRadiometer (MISR) and surface AOD observations from AErosol RObotic NETwork
45 (AERONET) shows reasonable agreements between simulated and observed AOD. However,
46 BCC-ESM1 shows weaker upward transport of aerosols from the surface to the middle and
47 upper troposphere, likely reflecting the deficiency of representing deep convective transport
48 of chemical species in BCC-ESM1. With an overall good agreement between BCC-ESM1
49 simulated and observed aerosol properties, it demonstrates a success of the implementation of
50 interactive aerosol and atmospheric chemistry in BCC-ESM1.

51

52 **1. Introduction**

53 Atmosphere is a thin gaseous layer around the Earth, consisting of nitrogen, oxygen and
54 a large number of trace gases including important greenhouse gases (GHG) such as water
55 vapor, tropospheric ozone (O_3), carbon dioxide (CO_2), methane (CH_4), nitrous oxide (N_2O),
56 and chloro-fluoro-carbons (CFCs). Besides gaseous components, atmosphere also contains
57 various aerosols, which are important for cloud formation and radiative transfer. Atmospheric
58 trace gases and aerosols are actually interactive components of the climate system. Their
59 inclusion in global climate models (GCMs) is a significant enhancement for most
60 state-of-the-art climate models (Lamarque et al., 2013; Collins et al., 2017). Early attempts in
61 coupling global climate dynamics with atmospheric chemistry can be traced back to late
62 1970s, when 3D transport of ozone and simple stratospheric chemistry were firstly
63 incorporated into a GCM to simulate global O_3 production and transport (e.g., Cunnold et al.
64 1975; Schlesinger and Mintz 1979). Since mid-1980s, a large number of on-line global
65 climate/chemistry models have been developed to address issues of the Antarctic stratospheric
66 O_3 depletion (e.g., Cariolle et al. 1990; Austin et al. 1992; Solomon, 1999), tropospheric O_3
67 and sulfur cycle (e.g., Feichter et al. 1996; Barth et al. 2000), tropospheric aerosol and its
68 interactions with cloud (e.g., Chuang et al. 1997; Lohmann et al. 2000; Ghan and Easter, 2006;
69 Jacobson 2012). Aerosols and chemically reactive gases in the atmosphere exert important
70 influences on global and regional air quality and climate (Collins et al., 2017).

71 Since 2013, the Beijing Climate Center (BCC), China Meteorological Administration,
72 has continuously developed and updated its fully-coupled GCM, the Beijing Climate Center
73 Climate System Model (BCC-CSM) (Wu et al., 2013; Wu et al., 2014; Wu et al., 2019).
74 BCC-CSM version 1.1 was one of the comprehensive carbon-climate models participating in
75 the phase five of the Coupled Model Intercomparison Project (CMIP5, Taylor et al. 2012).
76 When forced by prescribed historical emissions of CO_2 from combustion of fossil fuels and
77 land use change, BCC-CSM1.1 successfully reproduced the trends of observed atmospheric
78 CO_2 concentration and global surface air temperature from 1850 to 2005 (Wu et al., 2013).
79 During recent years, BCC-CSM1.1 has been used in numerous investigations on soil organic
80 carbon changes (e.g. Todd-Brown et al., 2014), ocean biogeochemistry changes (e.g. Mora et
81 al., 2013), and carbon-climate feedbacks (e.g. Arora et al., 2013; Hoffman et al., 2014).

82 BCC-CSM includes main climate-carbon cycle processes (Wu et al., 2013) and the global
83 mean atmospheric CO₂ concentration is calculated from a prognostic equation of CO₂ budget
84 taking into account global anthropogenic CO₂ emissions and interactive land-atmosphere and
85 ocean-atmosphere CO₂ exchanges.

86 In recent years, BCC has put large efforts in developing a global
87 climate-chemistry-aerosol fully-coupled Earth System Model (BCC-ESM1) on the basis of
88 BCC-CSM2 (Wu et al., 2019). The objective is to interactively simulate global aerosols (e.g.
89 sulfate, black carbon, etc.) and main greenhouse gases (e.g. O₃, CH₄, N₂O and CO₂) in the
90 atmosphere and to investigate feedbacks between climate and atmospheric chemistry.
91 BCC-ESM1 is at the point to be publicly released, and it is actively used by BCC for several
92 CMIP6-endorsed research initiatives (Eyring et al. 2016), including the Aerosol Chemistry
93 Model Intercomparison Project (AerChemMIP, Collins et al., 2017) and the Coupled
94 Climate–Carbon Cycle Model Intercomparison Project (C4MIP, Jones et al. 2016).

95 The purpose of this paper is to evaluate the performance of BCC-ESM1 in simulating
96 aerosols and their optical properties in the 20th century. The description of BCC-ESM1 is
97 presented in Section 2. The experimental protocol is given in Section 3. Section 4 presents the
98 evaluations of aerosol simulations with comparisons to CMIP5-recommended data (Lamarque
99 et al., 2010) and data obtained from both global surface networks and satellite observations.
100 The regional and global characteristics compared to observations and estimates from other
101 studies are analyzed. Simulations of aerosol optical properties in the 20th century are also
102 analyzed in Section 4. Conclusions and discussions are summarized in Section 5. Information
103 about code and data availability is given in Section 6.

104 **2. Model description**

105 BCC-ESM1 is an Earth System Model with interactive chemistry and aerosol
106 components, in which the atmospheric component is BCC Atmospheric General Model
107 version 3 (Wu et al., 2019) with interactive atmospheric chemistry (hereafter
108 BCC-AGCM3-Chem), land component BCC Atmosphere and Vegetation Interaction Model
109 version 2.0 (hereafter BCC-AVIM2.0), ocean component Modular Ocean Model version 4
110 (MOM4)-L40, and sea ice component [sea ice simulator (SIS)]. Different components of
111 BCC-ESM1 are fully coupled and interact with each other through fluxes of momentum,

112 energy, water, carbon and other tracers at their interfaces. The coupling between the
113 atmosphere and the ocean is done every hour.

114 The atmospheric component BCC-AGCM3-Chem is able to simulate global atmospheric
115 composition and aerosols from anthropogenic emissions as forcing agents. Its resolution is T42
116 (approximately $2.8125 \times 2.8125^\circ$ transformed spectral grid). The model has 26 levels in a hybrid
117 sigma/pressure vertical coordinate system with the top level at 2.914 hPa. Details of the model
118 physics are described in Wu et al. (2019). The BCC-AGCM3-Chem combines 66 gas-phase
119 chemical species and 13 bulk aerosol compounds as listed in Table 1. Apart from 3 gas-phase
120 species of dimethyl sulfide (DMS), sulfur dioxide (SO₂) and ammonia (NH₃), the other 63
121 gas-phase species are the same as those in the “standard version” of MOZART2 (Model for
122 Ozone and Related chemical Tracers, version 2), a global chemical transport model for the
123 troposphere developed by the National Center for Atmospheric Research (NCAR) driven by
124 meteorological fields from either climate models or assimilations of meteorological
125 observations (Horowitz et al., 2003). Advection of all tracers in BCC-AGCM3-Chem is
126 performed through a semi-Lagrangian scheme (Williamson and Rasch, 1989), and vertical
127 diffusion within the boundary layer follows the parameterization of Holtslag and Boville
128 (1993). The gas-phase chemistry of the 63 MOZART2 gas-phase species as listed in Table 1
129 is treated in the same way as that in the “standard version” of MOZART2 (Horowitz et al.,
130 2003), and there are 33 photolytic reactions and 135 chemical reactions involving 30 dry
131 deposited chemical species and 25 soluble gas-phase species. Dry deposition velocities for the
132 15 trace gases including O₃, carbon monoxide (CO), CH₄, formaldehyde (CH₂O), acetic acid
133 (CH₃OOH), hydrogen peroxide (H₂O₂), nitrogen dioxide (NO₂), nitric acid (HNO₃),
134 polyacrylonitrile (PAN), acetone (CH₃COCH₃), peroxyacetic acid (CH₃COOOH),
135 acetaldehyde (CH₃CHO), methylglyoxal (CH₃COCHO), nitric oxid (NO), and pernitric acid
136 (HNO₄) are not computed interactively and directly interpolated from MOZART2
137 climatological monthly mean deposition velocities
138 ([https://en.wikipedia.org/wiki/MOZART\(model\)](https://en.wikipedia.org/wiki/MOZART(model))) which are calculated offline (Bey et al., 2001;
139 Shindell et al., 2008) using a resistance-in-series scheme originally described in Wesely
140 (1989). The dry deposition velocities for the other 15 species including peroxy acetyl nitrate
141 (PAN), methyl nitroacetate (ONIT), organic nitrates (ONITR), ethyl alcohol (C₂H₅OH), organic

142 hydroxiperoxide (POOH), ethyl hydroperoxide (C_2H_5OOH), propylhydroperoxide
143 (C_3H_7OOH), methylene glycol mono acetate (ROOH), glycolaldehyde (GLYALD), acetol
144 (HYAC), methanol (CH_3OH), propanoic acid (MACROOH), isoprene hydroxy hydroperoxide
145 (ISOPOOH), carboxylic acid (XOOH), formaldehyde (HYDRALD), and hydrogen (H_2) are
146 calculated using prescribed deposition velocities of O_3 , CO, CH_3CHO , or land surface type
147 and surface temperature following the MOZART2 (Horowitz et al., 2003). Wet removal by
148 in-cloud scavenging for 25 soluble gas-phase species in the “standard version” of MOZART2
149 uses the parameterization of Giorgi and Chameides (1985) based on their temperature
150 dependent effective Henry’s law constants. In-cloud scavenging is proportional to the amount
151 of cloud condensate converted to precipitation, and the loss rate depends on the amount of
152 cloud water, the rate of precipitation formation, and the rate of tracer uptake by the liquid
153 phase water. Other highly soluble species such as HNO_3 , H_2O_2 , ONIT, ISOPOOH,
154 MACROOH, XOOH, and lead (Pb-210) are also removed by below-cloud washout as
155 calculated using the formulation of Brasseur et al. (1998). Below-cloud scavenging is
156 proportional to the precipitation flux in each model layer and the loss rate depends on the
157 precipitation rate. Vertical transport of gas tracers and aerosols due to deep convection is not
158 yet included in the present version of BCC-AGCM3-Chem, which process is considered as a
159 part of the deep convection and occurs generally in a small spatial region on a GCM-box with
160 low-resolution ($2.8^\circ lat. \times 2.8^\circ lon.$). Another consideration is that a large uncertainty exists to
161 treat transport of those water-soluble tracers by deep convection. But this effect will be
162 involved in the next version of BCC model.

163 The BCC-AVIM2.0 is the land model with terrestrial carbon cycle. It is described in
164 details in Li et al. (2019) and includes biophysical, physiological, and soil carbon-nitrogen
165 dynamical processes. The terrestrial carbon cycle operates through a series of biochemical
166 and physiological processes on photosynthesis and respiration of vegetation. Biogenic
167 emissions from vegetation are computed online in BCC-AVIM2.0 following the algorithm of
168 the Model of Emissions of Gases and Aerosols from Nature version 2.1 (MEGAN2.1,
169 Guenther et al., 2012).

170 The oceanic component of BCC-ESM1 is the Modular Ocean Model version 4 with 40
171 levels (hereafter MOM4-L40), and the sea ice component Sea Ice Simulator (SIS).

172 MOM4-L40 uses a tripolar grid of horizontal resolution with 1 °longitude by 1/3 °latitude
173 between 30 S and 30 N ranged to 1 °longitude by 1 °latitude from 60 S and 60 N poleward
174 and 40 z-levels in the vertical. Carbon exchange between the atmosphere and the ocean are
175 calculated online in MOM4-L40 using a biogeochemistry module that is based on the
176 protocols from the Ocean Carbon Cycle Model Intercomparison Project–Phase 2 (OCMIP2,
177 <http://www.ipsl.jussieu.fr/OCMIP/phase2/>). SIS has the same horizontal resolution as
178 MOM4-L40 and three layers in the vertical, including one layer of snow cover and two layers
179 of equally sized sea ice. Details of oceanic component MOM4-L40 and sea-ice component
180 SIS that are used in BCC-ESM1 may be found in Wu et al. (2013) and Wu et al. (2019).

181 In the following sub-sections, we will describe the treatments in BCC-ESM1 for 3
182 gas-phase species of DMS, SO₂ and NH₃, 13 prognostic aerosol species including sulfate
183 (SO₄²⁻), 2 types of organic carbon (hydrophobic OC1, hydrophilic OC2), 2 types of black
184 carbon (hydrophobic BC1, hydrophilic BC2), 4 categories of soil dust (DST01, DST02,
185 DST03, DST04), and 4 categories of sea salt (SSLT01, SSLT02, SSLT03, SSLT04).
186 Concentrations of all aerosols in BCC-ESM1 are mainly determined by advective transport,
187 emission, dry deposition, gravitational settling, and wet scavenging by clouds and
188 precipitation, except for SO₄²⁻ which gas-phase and aqueous phase conversion from SO₂ are
189 also considered. The present version of aerosol scheme belongs to a bulk aerosol model and
190 mainly refers to the scheme of CAM-Chem (Lamarque et al., 2012), but the nucleation and
191 coagulation of aerosols are still ignored.

192 **2.1 SO₂, DMS, NH₃, and Sulfate**

193 SO₂ is a main sulfuric acid precursor to form aerosol sulfate SO₄²⁻. Conversions of SO₂
194 to SO₄²⁻ occur by gas phase reactions (Table 2) and by aqueous phase reactions in cloud
195 droplets. The dry deposition velocity of SO₂ follows the resistance-in-series approach of
196 Wesely (1989) using the formula, $W_{SO_2} = 1/(r_a + r_b + r_c)$, in which r_a , r_b , and r_c are the
197 aerodynamic resistance, the quasi-laminar boundary layer resistance, and the surface
198 resistance, respectively and they are interactively computed in each model time step. The loss
199 rate of SO₂ due to wet deposition is computed following the scheme in the global Community
200 Atmosphere Model (CAM) version 4, the atmospheric component of the Community Earth
201 System Model (Lamarque et al., 2012).

202 The sources of SO₂ mainly come from fuel combustion, industrial activities, and
203 volcanoes. SO₂ can also be formed from the oxidation of DMS as listed in Table 2 in which
204 their reaction rates follow CAM-Chem (Lamarque et al. 2012). The main source of DMS is
205 from oceanic emissions via biogenic processes. It is prescribed with the climatological
206 monthly data that are extracted from MOZART2 package
207 (<https://www2.acom.ucar.edu/gcm/mozart-4>). SO₄²⁻ is one of the prognostic aerosols in
208 BCC-AGCM3-Chem. Its treatment follows CAM4-Chem (Lamarque et al., 2012). It is
209 produced primarily by the gas-phase oxidation of SO₂ (in Table 2) and by aqueous phase
210 oxidation of SO₂ in cloud droplets. The gas phase reactions, rate constants, and gas-aqueous
211 equilibrium constants are given by Tie et al. (2001). The heterogeneous reactions of SO₄²⁻
212 occur on all aerosol surfaces. Their treatment follows a Bulk Aerosol Model (BAM) used in
213 CAM4 (Neale et al., 2010). The heterogeneous reactions depend strongly on pH values in
214 clouds which are calculated from the concentrations of SO₂, HNO₃, H₂O₂, NH₃, O₃, HO₂, and
215 SO₄²⁻. NH₃ is a gas tracer apart from MOZART2 (Table 1). Its sources include aircraft and
216 surface emissions due to anthropogenic activity, biomass burning, and biogenic emissions
217 from land soil and ocean surfaces (Table 4). SO₄²⁻ is assumed to be all in aqueous phase due
218 to water uptake, although Wang et al. (2008a) showed that ~34% of sulfate particles are in
219 solid phase globally due to the hysteresis effect of ammonium sulfate phase transition.
220 However, in terms of radiative forcing, consideration of solid sulfate formation process
221 lowers the sulfate forcing by ~8% as compared to consideration of all sulfate particles in
222 aqueous phase (Wang et al., 2008b). Future model development may consider the life cycle of
223 NH₃. The sulfate in- and below-cloud scavenging follows Neu and Prather (2011). Washout
224 of SO₄²⁻ is set to 20% of the washout rate of HNO₃ following Tie et al. (2005) and Horowitz
225 (2006). Dry deposition velocity of SO₄²⁻ is also calculated by the resistance-in-series
226 approach.

227 **2.2 Aerosols of organic carbon and black carbon**

228 BCC-AGCM3-Chem treats two types of organic carbon (OC), i.e. water-insoluble tracer
229 OC1 and water-soluble tracer OC2, and two types of black carbon (BC), i.e. water-insoluble
230 tracer BC1 and water-soluble tracer BC2. As shown in Table 2, hydrophobic BC1 and OC1
231 can be converted to hydrophilic BC2 and OC2 with a constant rate of $7.1 \times 10^{-6} \text{ s}^{-1}$ (Cooke and

232 Wilson, 1996). The 4 tracers of organic carbon and black carbon are mainly from emissions
233 including both fossil fuel and biomass burning, and are from the CMIP6 data package
234 (<https://esgf-node.llnl.gov/search/input4mips/>, Hoesly et al., 2018). Beside anthropogenic and
235 biomass burning emissions, hydrophilic organic carbon OC2 can also come from natural
236 biogenic volatile organic compound (VOC) emissions. Dry deposition velocities for all the 4
237 OC and BC tracers are set to $0.001\text{m}\cdot\text{s}^{-1}$. OC2 and BC2 are soluble aerosols, and their sinks
238 are primarily governed by wet deposition. Their in- and below-cloud scavenging follows the
239 scheme of Neu and Prather (2011).

240 **2.3 Sea salt aerosols**

241 As shown in Table 3, sea salt aerosols in the model are classified into four size bins (0.2–
242 1.0, 1.0–3.0, 3.0–10, and 10–20 μm) in diameter. They originate from oceans and are
243 calculated online by BCC-ESM1. The upward flux $F_{sea-salt}$ of sea salt productions for four
244 bins is proportional to the 3.41 power of the wind speed u_{10m} at 10 m height near the sea
245 surface (Mahowald et al., 2006) and is expressed as

$$246 \quad F_{sea-salt} = S \cdot (u_{10m})^{3.41}, \quad (1)$$

247 where S is a scaling factor and set to 4.05×10^{-15} , 4.52×10^{-14} , 1.15×10^{-13} , 1.20×10^{-13} for four
248 size bins of sea salt aerosols in BCC-ESM1, respectively.

249 Dry deposition of sea salts depends on the turbulent deposition velocity in the lowest
250 atmospheric layer using aerodynamic resistance and the friction velocity, and the settling
251 velocity through the whole atmospheric column for each bin of sea salts. The turbulent
252 deposition velocity and settling velocity depend on particle diameter and density (listed in
253 Table 3). In addition, the fact that the size of sea salts changes with humidity is also
254 considered. The wet deposition of sea salts follows the scheme for soluble aerosols used in
255 CAM4, and depends on prescribed solubility and size-independent scavenging coefficients.

256 **2.4 Dust aerosols**

257 Dust aerosols behave in a similar way as sea salts. Their variations involve three major
258 processes: emission, advective transport, and wet/dry depositions. The dust emission is based
259 on a saltation-sandblasting process, and depends on wind friction velocity, soil moisture, and
260 vegetation/snow cover (Zender et al., 2003). The vertical flux of dust emission is corrected by
261 a surface erodible factor at each model grid cell which has been downloaded from NCAR

262 website (<https://svn-ccsm-inputdata.cgd.ucar.edu/trunk/inputdata/atm/cam/dst/>). Soil
 263 erodibility is prescribed by a physically-based geomorphic index that is proportional to the
 264 runoff area upstream of each source region (Albani et al., 2014). Like sea salts, dry deposition
 265 of dust aerosols includes gravitational and turbulent deposition processes, while wet
 266 deposition results from both convective and large scale precipitation and is dependent on
 267 prescribed size-independent scavenging coefficients.

268 **2.5 Effects of aerosols on radiation, clouds, and precipitation**

269 The mass mixing ratios of bulk aerosols are prognostic variables in BCC-ESM1 and
 270 directly affect the radiative transfer in the atmosphere with their treatments following the
 271 NCAR Community Atmosphere Model (CAM3, Collins et al., 2004). Indirect effects of
 272 aerosols are taken into account in the present version of BCC-AGCM3-Chem (Wu et al.,
 273 2019). Aerosol particles act as cloud condensation nuclei and exert influence on cloud
 274 properties and precipitation, and ultimately impact the hydrological cycle. Prognostic aerosol
 275 masses are used to estimate the liquid cloud droplet number concentration N_{cdnc} (cm^{-3}) in
 276 BCC-AGCM3-Chem. N_{cdnc} is explicitly calculated using the empirical function suggested
 277 by Boucher and Lohmann (1995) and Quaas et al. (2006):

$$278 \quad N_{cdnc} = \exp\left[5.1 + 0.41 \ln(m_{aero})\right] \quad (2)$$

279 where m_{aero} ($\mu\text{g}\cdot\text{m}^{-3}$) is the total mass of all hydrophilic aerosols,

$$280 \quad m_{aero} = m_{SS} + m_{OC} + m_{SO_4} + m_{NH_4NO_2}, \quad (3)$$

281 i.e. the first bin of sea salt (m_{SS}), hydrophilic organic carbon (m_{OC}), sulphate (m_{SO_4}), and
 282 Ammonium nitrite (NH_4NO_2). A dataset of NH_4NO_2 from NCAR CAM-Chem (Lamarque et
 283 al., 2012) is used in our model.

284 N_{cdnc} is an important factor in determining the effective radius of cloud droplets for
 285 radiative calculation. The effective radius of cloud droplets r_{el} is estimated as

$$286 \quad r_{el} = \beta \cdot r_{l,vol}, \quad (4)$$

287 where β is a parameter dependent on the droplets spectral shape and follows the calculation
 288 proposed by Peng and Lohmann (2003),

$$289 \quad \beta = 0.00084 N_{cdnc} + 1.22. \quad (5)$$

290 $r_{l,vol}$ is the volume-weighted mean cloud droplet radius,

$$291 \quad r_{l,vol} = \left[(3LWC) / (4\pi\rho_w N_{cdnc}) \right]^{1/3}, \quad (6)$$

292 where ρ_w is the liquid water density and LWC the cloud liquid water content (g cm^{-3}).

293 Aerosols also exert impacts on precipitation efficiency (Albrecht, 1989), which is taken
 294 into account in the parameterization of non-convective cloud processes. There are five
 295 processes that convert condensate to precipitate: auto-conversion of liquid water to rain,
 296 collection of cloud water by rain, auto-conversion of ice to snow, collection of ice by snow,
 297 and collection of liquid by snow. The auto-conversion of cloud liquid water to rain ($PWAUT$)
 298 is dependent on the cloud droplet number concentration and follows a formula that was
 299 originally suggested by Chen and Cotton (1987),

$$300 \quad PWAUT = C_{l,aut} \hat{q}_l^2 \rho_a / \rho_w \left(\frac{q_l \rho_a}{\rho_w N_{ncdc}} \right)^{1/3} H(r_{l,vol} - r_{lc,vol}) \quad (7)$$

301 Where \hat{q}_l is in-cloud liquid water mixing ratio, ρ_a and ρ_w are the local densities of air and
 302 water respectively, and $C_{l,aut}$ is a constant. $H(x)$ is the Heaviside step function with the
 303 definition,

$$304 \quad H(x) = \begin{cases} 0, & x < 0 \\ 1, & x \geq 0 \end{cases}. \quad (8)$$

305 $r_{lc,vol}$ is the critical value of mean volume radius of liquid cloud droplets $r_{l,vol}$, and set to 15
 306 μm .

307 The treatment of aerosol single scattering (optical) properties (such as mass extinction
 308 efficiency, single scattering albedo, and asymmetric factor) follows the look-up table
 309 approach in CAM (Collins et al., 2004). The optics for black, organic carbon, sea salt, and sea
 310 salt particles is assumed to be same as the optics for soot and water-soluble aerosols in the
 311 Optical Properties of Aerosols and Clouds (OPAC) data set (Hess et al., 1998). The optics for
 312 dust is derived by Mie calculations for the size distribution represented by each size bin
 313 (Zender et al., 2003). Similarly, for sulfate and nitrate particles, same set of aerosol optical
 314 properties for ammonium sulfate are used and are taken from Wang et al. (2008b) with
 315 treatment of aerosol hygroscopicity. The volcanic stratospheric aerosols are assumed to be
 316 comprised of 75% sulfuric acid and 25% water, as in Hess et al. (1998). For each model year,

317 different aerosol types are assumed to be externally mixed in the calculation of bulk aerosol
318 single scattering properties that are in turn used in the radiative transfer calculations.

319 **3. Experiment design for the 20th century climate simulation**

320 There is an Aerosol Chemistry Model Intercomparison Project (AerChemMIP, Collins et
321 al., 2017) endorsed by the Coupled-Model Intercomparison Project 6 (CMIP6) for
322 documenting and understanding past and future changes in the chemical composition of the
323 atmosphere, and estimating the global-to-regional climate response from these changes.
324 Modelling groups with full chemistry and aerosol models are encouraged to perform all
325 AerChemMIP simulations (Collins et al., 2017). To assess the ability of our model to simulate
326 aerosols (mean and variability), we have followed the historical simulation designed by
327 CMIP6 (Eyring et al., 2016) which is named as “historical” experiment in the Earth System
328 Grid Federation (ESGF). The historical experiment is forced with emissions evolving from
329 1850 to 2014 that include biomass burning emissions (Van Marle et al. 2017), anthropogenic
330 and open burning emissions (Hoesly et al., 2018; Feng et al., 2019). O₃ in the historical
331 simulation is an interactive prognostic variable and feedbacks on radiation, and the
332 concentrations of other WMOGHG, e.g. CH₄, N₂O, CO₂, CFC11, and CFC12 are prescribed
333 using CMIP6 historical forcing data (Meinshausen et al., 2017). Although CH₄ and N₂O are
334 prognostic variables in the chemistry scheme (Table 1), their prognostic values at each model
335 step in the historical experiment are replaced by CMIP6 data (Meinshausen et al., 2017)
336 throughout the model domain. The rest of historical forcing data include: (1) yearly global
337 gridded land-use forcing data sets (Hurtt et al., 2011; Hurtt et al., 2017), and (2) solar forcing
338 (Matthes et al., 2017). All these datasets were downloaded from
339 <https://esgf-node.llnl.gov/search/input4mips/>. Climate feedback processes that involve
340 changes to the atmospheric composition of reactive gases and aerosols may affect the
341 temperature response to a given WMOGHG concentration level.

342 **3.1 Surface emissions**

343 Surface emissions of chemical species from different sources are summarized in Table
344 4. They include anthropogenic emissions from fossil fuel burning and other industrial
345 activities, biomass burning (including vegetation fires, fuel wood and agricultural burning),
346 biogenic emissions from vegetation and soils, and oceanic emissions. Most historical

347 emissions from anthropogenic source (surface, aircraft plus ship) and biomass burning from
348 1850 to 2014 are CMIP6-recommended data (available at
349 <https://esgf-node.llnl.gov/search/input4mips>). Anthropogenic or biomass burning sources of
350 some tracers which are not included in the CMIP6 dataset (see Table 4), anthropogenic
351 emission of H₂ and N₂O are from monthly climatological dataset provided by the MOZART-2
352 standard package. N₂O is a prognostic variable in BCC-ESM1 but it is replaced by CMIP6
353 prescribed concentration in the historical run. Other emissions including biomass burning
354 (CH₃COCH₃) and anthropogenic emission (CH₃CHO, CH₃OH, and CH₃COCH₃) are from the
355 Atmospheric Chemistry and Climate Model Intercomparison Project (ACCMIP) emission
356 inventory (<http://accent.aero.jussieu.fr/ACCMIP.php>) covering the period from 1850 to 2010
357 with 10-year intervals (see Table 4). Monthly lumped emissions of black carbon and organic
358 carbon aerosols from 1850 to 2014 are downloaded from CMIP6-recommended data, but we
359 used 80% (for BC) and 50% (for OC) of them in their hydrophobic forms (BC1 and OC1) and
360 the rest in their hydrophilic forms (BC2 and OC2), following the work of Chin et al. (2002).

361 Five tracers of ISOP, ACET (CH₃COCH₃), C₂H₄, C₃H₈, and Monoterpenes (C₁₀H₁₆) in
362 Table 1 belong to biogenic volatile organic carbons (VOCs). As shown in Table 4, those
363 VOCs emissions are online calculated in BCC-ESM1 following the modeling framework of
364 the Model of Emissions of Gases and Aerosols from Nature version 2.1 (MEGAN2.1,
365 Guenther et al., 2012) using simple mechanistic algorithms to account for major known
366 processes controlling biogenic emissions. The MEGAN2.1 can provide a flexible scheme for
367 estimating 16 tracers of biogenic emissions from terrestrial ecosystems including five VOCs
368 emissions used in BCC-ESM1 (Table 4). All the VOCs emissions depend on current and past
369 surface air temperature, solar flux, and the landscape types. Their calculation requires global
370 maps of plant functional type (PFT) and leaf area index (LAI) which is a prognostic variable
371 from the land model BCC-AVIM2. The effect of atmospheric CO₂ concentration on isoprene
372 emissions is included. 10% of the biogenic monoterpenes emissions as calculated online with
373 the MEGAN2.1 algorithm in BCC-AVIM2 are converted to hydrophilic organic carbon (OC2)
374 to account for formation of secondary organic aerosols following Chin et al. (2002) in this
375 version of BCC-ESM1.

376 **3.2 Volcanic eruptions, lightning and aircraft emissions**

377 As there is no stratospheric aerosol scheme in BCC-ESM1, concentrations of sulfate
378 aerosol at heights from 5 to 39.5 km, which volcanic origin, are directly prescribed using the
379 CMIP6-recommended data (Thomasson et al., 2018) from 1850 to 2014. The effects of
380 surface SO₂ emissions from volcanic eruption on the variation of SO₂ in the atmosphere and
381 then on the variation of tropospheric SO₄²⁻ concentration are considered, and the SO₂
382 emissions from 1850 to 2014 are downloaded from the IPCC ACCMIP emission inventory
383 (<http://accent.aero.jussieu.fr/ACCMIP.php>). Aircraft emissions are provided for NO₂, CO,
384 CH₄, NH₃, NO, SO₂, and aerosols of OC and BC (Table 1). The emissions of NO from
385 lightning are online calculated in BCC-AGCM3-Chem following the parameterization in
386 MOZART2, and the globally-averaged mean during the period of 1850 to 2014 is 5.19
387 Tg(N) yr⁻¹, which is in agreement with observations within the range of 3 to 6 Tg(N) yr⁻¹
388 (Martin et al., 2002). The lightning frequency depends strongly on the convective cloud top
389 height, and the ratio of cloud-to-cloud versus cloud-to-ground lightning depends on the cold
390 cloud thickness from the level of 0°C to the cloud top (Price and Rind, 1992).

391 **3.3 Upper boundary of the atmosphere**

392 As no stratospheric chemistry is included in the present version of BCC-AGCM3-Chem,
393 it is necessary to ensure a proper distribution of chemically-active stratospheric species.
394 Concentrations of different tracers (O₃, CH₄, N₂O, NO, NO₂, HNO₃, CO, and N₂O₅) at the top
395 two layers of the model are set to prescribed monthly climatological values, and
396 concentrations from below the top two layers to the tropopause are relaxed at a relaxation
397 time of 10-days towards the climatology. Climatological values of NO, NO₂, HNO₃, CO and
398 N₂O₅ at the top two layers are extracted from MOZART2 data package available at the
399 Website (<https://www2.acom.ucar.edu/gcm/mozart-4>), originated from the Study of Transport
400 and Chemical Reactions in the Stratosphere (STARS, Brasseur et al., 1997). Concentrations
401 for the other tracers (O₃, CH₄, and N₂O) at the top two model layers are the zonally-averaged
402 and monthly values from 1850 to 2014 derived from the CMIP6 data package.

403 **3.4 The preindustrial model states**

404 The preindustrial state of BCC-ESM1 is obtained from a piControl simulation of over 600
405 years in which all forcings including emissions data are fixed at 1850 conditions. The initial
406 state of the piControl simulation itself is obtained through individual spin-up runs of each

407 component of BCC-ESM1 in order for the piControl simulation to run stably and fast to reach
408 its equilibrium. Figures 1(a-c) show the time series of global yearly means of the net energy
409 budget at top of the atmosphere (TOA), near-surface air temperature (TAS), and sea surface
410 temperature (SST) from the piControl simulation for the last 450 years. It shows that the
411 surface climate in BCC-ESM1 nearly reaches its equilibrium after 600 years piControl
412 simulation. The whole system in BCC-ESM1 fluctuates around $+0.7 \text{ Wm}^{-2}$ net energy flux at
413 TOA without obvious trend in 450 years (Fig. 1a). This level of TOA energy imbalance is
414 close to the average imbalance (1.0 Wm^{-2}) among CMIP5 models (Wild et al., 2013). It means
415 that there exists surplus energy of $+0.7 \text{ Wm}^{-2}$ obtained by the whole system in BCC-ESM1,
416 but do not cause remarkable climate drift. The global mean TAS and SST keep around 288.1
417 K (Fig. 1b) and 295.05 K (Fig. 1c), respectively. During the last 450 years, there are ($\pm 0.2 \text{ K}$
418 amplitude of TAS and SST) oscillations of centennial scale for the whole globe (Figs. 1b and
419 1c), which are certainly caused by internal variation of the system.

420 Figures 2a-2c show the time series of global annual total burdens of SO_2 , DMS, and OH
421 in the troposphere (integrated from the surface to 100 hPa) in the last 450 years of the
422 piControl simulation. Without any anthropogenic source, the SO_2 amount in the troposphere
423 nearly keeps the level of 0.0868 Tg in the 450 years of the piControl simulation. Tropospheric
424 DMS varies around the value of 0.116 Tg. Tropospheric OH, as an important gas species
425 oxidizing SO_2 to form SO_4^{2-} (Table 2), keeps at a stable level in the atmosphere. SO_4^{2-} also
426 remains at a stable level of 0.556 Tg in the atmosphere in the whole period of the piControl
427 simulation (Figure 2d). The amounts of BC and OC in the troposphere vary around 0.0395 Tg
428 and 0.275 Tg (Figures 2e-2f), respectively. Dust and sea salt aerosols are at the level of 22 Tg
429 and 11.7 Tg (Figures 2g-2h), respectively. All those data are close to the global mean
430 concentrations of 0.604 Tg SO_4^{2-} , 0.046 Tg BC, 0.30 Tg OC, 22.18 Tg dust, and 11.73 Tg sea
431 salts in 1850 which are estimated based on the CMIP5 prescribed data in 1850 (Lamarque et
432 al., 2010).

433 Figure 3 shows the global spatial distributions of annual mean sulfate, organic carbon,
434 black carbon, dust, and sea salt aerosols in the whole atmospheric column averaged for the
435 last 100 years of the piControl simulation of BCC-ESM. We can compare them with CMIP5
436 recommended concentrations in year 1850, considered as the reference state in the

437 pre-industrial stage. At that time, there are fewer anthropogenic/biomass SO₂ emissions, the
438 SO₄²⁻ over land are evidently smaller than those over oceans especially over the tropical
439 Pacific and Atlantic Oceans, where DMS can be oxidized to SO₂ and then form SO₄²⁻. There
440 are several centers of high values of black carbon and organic carbon in East and South Asia,
441 Europe, Southeast America, and in the tropical rain forests in Africa and South America.
442 They mainly result from biomass burning including vegetation fires, fuel wood and
443 agricultural burning. Dust aerosols are mainly distributed in North Africa, Central Asia, North
444 China, and Australia, where arid and semi-arid areas locate. Dust emitted from Sahara Desert
445 can be transported to the tropical Atlantic by easterly wind. The sea salt aerosols are mainly
446 distributed over the mid-latitude Southern Oceans, the tropical southern Indian Ocean, and the
447 tropical northern Pacific Ocean, where wind speeds near the sea surface are strong. As shown
448 in Fig. 3, all the spatial distribution patterns of CMIP5-derived sulfate, black carbon, organic
449 carbon, dust, and sea salt aerosols (Lamarque et al., 2010) are well simulated in BCC-ESM1.
450 There are high spatial correlation coefficients, 0.76 for sulfate, 0.77 for black carbon, 0.77 for
451 organic carbon, 0.94 for dust, and 0.94 for sea salts, between CMIP5 data and BCC-ESM1
452 simulations. Relative lower relations for sulfate, black carbon and organic carbon are possibly
453 caused as different anthropogenic emission sources are used in BCC-ESM1 and to create
454 CMIP5 data. Dust and sea salts belong to natural aerosols and depend on the land and sea
455 surface conditions, so their spatial distributions are easy to be captured and have relatively
456 higher correlations between CMIP5 data and BCC-ESM1 simulations.

457

458 **4. Evaluation of O₃ and aerosol simulations in the 20th century**

459 The rate of sulfate formation is dependent on the levels of oxidants in the troposphere.
460 O₃ is an important oxidant. So, the evaluation of simulated tropospheric O₃ is helpful to
461 understand the aerosols simulations. BCC-ESM1 is driven by most of the
462 CMIP6-recommended emission data. As shown in Figure 4, the zonal distributions of the total
463 amounts of tropospheric O₃ below 300 hPa to the ground and their changes with time from
464 1850 to 2014 from the CMIP6-recommend dataset (Table 4) are well simulated by
465 BCC-ESM1. Evident increasing trends since 1850 almost exist in every latitudes, especially
466 in the Northern Hemisphere where the contents of tropospheric O₃ are higher than those in the

467 Southern Hemisphere.

468 Figure 5 shows the vertical profiles of O₃ simulations with comparison to global
469 ozonesonde observations averaged for the monthly data over 2010-2014 from the World
470 Ozone and Ultraviolet Radiation Data Centre (WOUDC; <http://woudc.org/data.php>, last
471 access: 24 September 2019) in nine regions which are averaged from 41 global WOUDC sites.
472 The details of WOUDC data may refer to Lu et al. (2019). As shown in Figure 5, BCC-ESM1
473 well captures the observed ozone vertical structure at all regions. At the lower and middle
474 troposphere (i.e. below 6 km), the model typically shows positive bias within 5 ppbv for the
475 Southern Hemisphere and 10 ppbv for the Northern mid-latitudes, similar to those simulated
476 from many other global atmospheric chemical models (Young et al., 2013, 2018). The model
477 has larger ozone overestimation in the upper troposphere and stratosphere at most regions, at
478 least partly due to the use of prescribed stratospheric ozone as upper boundary conditions
479 and/or errors in modeling ozone exchange between the stratosphere and the troposphere.
480 Global tropospheric ozone burden derived from our simulation is 335 Tg averaged over
481 2010-2014, in consistent with recent assessment from multi chemistry models (Young et al.,
482 2018).

483 **4.1 Global aerosols trends**

484 Figure 6(a)-(c) show the time series of global total emissions of SO₂, OC, and BC to the
485 atmosphere from natural and anthropogenic sources. Emissions of SO₂ are largely due to
486 industrial production. From 1850 to 1915, SO₂ emissions increased year by year as the
487 Industrial Revolution intensified and expanded. But from 1915 to 1945, the increase trend of
488 SO₂ emissions became slower as broke out the First and the Second World Wars. After that
489 period, with growing industrial productions, SO₂ emissions increased again and reached a
490 maximum around the end of 1970s. During the 1980s and 2000s, with a substantial decrease
491 of SO₂ emissions in Europe and the United States, the global SO₂ emissions has been
492 decreasing since the 1980s despite the rapid increase of SO₂ emissions in South and East Asia
493 as well as in developing countries in the Southern Hemisphere in recent years (Liu et al.,
494 2009). The OC and BC emissions substantially increased since 1950s just after the Second
495 World War. The global total OC emission in 2010 was nearly twice as much as that in
496 pre-industrial (year 1850) and increased by 18 Tg • yr⁻¹. Anthropogenic black carbon

497 emissions increased from 1 Tg yr⁻¹ in 1850 to nearly 8 Tg yr⁻¹ in 2010.

498 Anthropogenic SO₂, OC and BC emissions strongly affect the variations of atmospheric
499 concentrations of sulfate, OC, and BC. The global 0.5°x0.5° gridded data of
500 CMIP5-recommended aerosols masses with 10-years interval from 1850 to 2000 (Lamarque
501 et al., 2010) provides an important reference to evaluate the aerosol simulations in
502 BCC-ESM1. As shown in Figure 7b-7f, the annual total aerosol burdens of SO₄²⁻, OC, and BC
503 in the whole atmosphere column as simulated by the BCC-ESM1 20th century historical
504 simulation are generally consistent with the values derived from CMIP5-recommended
505 aerosols concentrations. Due to increasing SO₂ emissions from 1850 to present day (Fig. 6),
506 the global SO₂ burden in the atmosphere increased from 100 Tg in 1850s to 200 Tg in 1980s
507 (Fig. 7a), and has a high correlation coefficient of 0.996 with the anthropogenic emissions
508 (Fig. 6a), as the lifetime of SO₂ is short. The burden directly followed the emission. DMS in
509 the atmosphere is oxidized by OH and NO₃ to form SO₂ (Table 2). Its natural emissions from
510 oceans from 1850 to 2010 in the model are the climatological monthly means (Dentener et al.,
511 2006) from MOZART2 data package. As shown in Fig 7a, the global amount of DMS in the
512 whole atmosphere was about 0.12 Tg during 1850-1900 and decreased to 0.055 Tg in 2010.
513 This decrease trend maybe partly results from the speeded rate of DMS oxidation with global
514 warming, and the loss of DMS gradually exceeds the source of ocean DMS emission to cause
515 a net loss of DMS in the atmosphere since 1910s. Largely driven by SO₂ anthropogenic
516 emissions, the sulfate burden shows three different stages from 1850 to present. In the first
517 period from 1850s to 1900s, the sulfate burden had a weak linear increase. It increased
518 significantly in the second stage from 1910's to 1940's, and then exploded since 1950's, until
519 the middle 1970s and early 1980s. The sulfate burden then remained nearly stable and even
520 showed slightly decreases as seen from the CMIP5 data. As for global BC and OC burdens,
521 BCC-ESM1 results show continuous increases since 1850s, especially from 1950 to present.
522 From 1910's to 1940's, the CMIP5 data show a slight decrease of BC and OC burdens in the
523 atmosphere.

524 The dust and sea salt aerosols in the atmosphere are largely determined by the
525 atmospheric circulations and states of the land and ocean surface. We can see that the global
526 dust burden in the atmosphere showed evident increase from 1980 to 2000, which could be

527 partly caused by evident global warming since 1980 and increasing soil dryness resulting in
528 more surface dust to be released in the atmosphere. Their details will be explored in the other
529 paper.

530 **4.2 Global aerosols budgets**

531 We further evaluate global aerosols budgets by comparing a 10-year average of
532 BCC-ESM results from 1990 to 2000 with various studies for sulfate, BC, OC, sea salt, and
533 dust. Their annual total emissions, average atmospheric mass loading, and mean lifetimes are
534 listed in Tables 5 and 6. It is worth emphasizing that the global mean total source and sink for
535 each type of aerosols in BCC-ESM1 are almost balanced.

536 The global DMS emission from the ocean is $27.4 \text{ Tg(S) yr}^{-1}$ in BCC-ESM. This
537 emission in BCC-ESM is nearly balanced by the gas-phase oxidation of DMS to form SO_2 .
538 The DMS burden is 0.12 Tg with a lifetime of 0.78 days, which is within the range of other
539 models reported in the literature. As shown in Table 5, the total SO_2 production averaged for
540 the period of 1991 to 2000 is $76.93 \text{ Tg(S) yr}^{-1}$. A rate of $13.2 \text{ Tg(S) yr}^{-1}$ (about 17%) SO_2 is
541 produced from the DMS oxidation, only $0.1 \text{ Tg(S) yr}^{-1}$ SO_2 from airplane emissions to the
542 atmosphere, and the rest ($63.63 \text{ Tg(S) yr}^{-1}$, near 82.7%) from anthropogenic activities and
543 volcanic eruption at surface. The amount of SO_2 produced from the DMS oxidation is in the
544 range of other works (10.0 to $24.7 \text{ Tg(S) yr}^{-1}$) reported in Liu et al (2005). All the SO_2
545 production is balanced by SO_2 losses by dry and wet deposition, and by gas- and
546 aqueous-phase oxidation. Half of its loss ($38.74 \text{ Tg(S) yr}^{-1}$) occurs via its aqueous-phase
547 oxidation to form sulfate. Other losses through dry and wet depositions and gas-phase
548 oxidation to form SO_4^{2-} are also important (Table 2). All the sinks are in the range from the
549 literature (Liu et al., 2005). The global burden of SO_2 in the atmosphere is 0.48 Tg with a
550 lifetime of 1.12 days, consistent with values in literature (Liu et al., 2005).

551 Sulfate aerosol is mainly produced from aqueous-phase SO_2 oxidation ($38.73 \text{ Tg(S) yr}^{-1}$)
552 and partly from gaseous phase oxidation of SO_2 ($10.32 \text{ Tg(S) yr}^{-1}$), and is largely lost by wet
553 scavenging ($49.06 \text{ Tg(S) yr}^{-1}$). The total SO_4^{2-} production in BCC-ESM is at the lower range
554 of values in other models reported in Textor et al. (2006). Its global burden is 1.89 Tg and the
555 lifetime is 4.69 days, which are within the range of 1.71 to 2.43 Tg and 3.3 to 5.4 days in the
556 literatures (Textor et al., 2006; Liu et al., 2012; Liu et al., 2016; Matsui and Mahowald, 2017;

557 Tegen et al., 2019; the value derived from CMIP5 data).

558 Sources of BC and OC are mainly from anthropogenic emissions. Based on the CMIP6
559 data, there are, on average, 7.22 Tg yr⁻¹ BC and 13.91 Tg yr⁻¹ OC from fossil and bio-fuel
560 emissions and 18.38 Tg yr⁻¹ OC from natural emission during the period of 1991 to 2000.
561 Most of them are scavenged through convective and large-scale rainfall processes. The rest
562 returns to the surface by dry deposition. The simulated global BC and OC burdens are 0.13
563 and 0.62 Tg, respectively (Table 6), all close to values of 0.114 Tg BC and 0.69 Tg OC
564 derived from the CMIP5 data, and within the range of 0.11-0.26 Tg BC (Textor et al., 2006;
565 Matsui and Mahowald, 2017; Tegen et al., 2019) and less than the values of 1.25-2.2 Tg OC
566 in other literatures (Textor et al., 2006; Tegen et al., 2019). The simulated BC and OC
567 lifetimes are 6.6 and 5.0 days respectively, and are close to the recent values of 5.0-7.5 days
568 BC and 5.4-6.6 days OC in literatures (Matsui and Mahowald, 2017; Tegen et al., 2019).

569 The emissions of dust and sea salt are mainly determined by winds near the surface. The
570 annual total dust emission in BCC-ESM1 is 2592 Tg yr⁻¹, higher than AeroCom multi-model
571 mean (1840 Tg yr⁻¹, Textor et al., 2006), but comparable to other studies (Chin et al., 2002;
572 Liu et al., 2012; Matsui and Mahowald, 2017). The average dust loading is 22.93 Tg, lower
573 than the value of 35.9 Tg in Ginoux et al. (2001) but slightly higher than the value of 20.41
574 Tg derived from CMIP5 data. The average lifetime for dust particles is 3.23 days that is
575 shorter than the AeroCom mean (4.14 days) and the value of 3.9 days in recent study (Matsui
576 and Mahowald, 2017). The simulated sea salt emission is 4667.2 Tg yr⁻¹, slightly lower than
577 the simulated value in Liu et al. (2012), and substantially lower than the AeroCom mean
578 (16600 Tg yr⁻¹, Textor et al., 2006). The simulated sea salt burdens are 11.89 Tg and close to
579 the CMIP5 data. Their averaged lifetimes are 0.93 days and close to the value in the recent of
580 Matsui and Mahowald (2017) but longer than the AeroCom mean (0.41days, Textor et al.,
581 2006).

582 **4.3 Global aerosol distributions at present day**

583 Figures 8-12 show December-January-February (DJF) and June-July-August (JJA) mean
584 column mass concentrations of sulfate (SO₄²⁻), OC, BC, Dust, and Sea Salt aerosols averaged
585 for the period of 1991-2000, respectively. Here, BCC-ESM1 simulated results are compared
586 with the CMIP5-recommended data for the same period. Unlike the pre-industrial level of

587 sulfate shown in Fig. 2, sulfate concentrations at present day (Fig. 8) are strongly influenced
588 by anthropogenic emissions, and have maximum concentrations in the industrial regions (e.g.,
589 East Asia, Europe, and North America). Their seasonal variations are distinct and are
590 characterized by high concentrations in boreal summer and low concentrations in boreal
591 winter. These spatial distributions simulated by BCC-ESM1 are well consistent with the
592 CMIP5 data, with spatial correlation coefficients in DJF and JJA reaching 0.92 and 0.83
593 (Figure 13), respectively. The deviation of the spatial pattern in BCC-ESM1 is less from the
594 CMIP5 data in DJF but larger in JJA (Figure 13).

595 Unlike sulfate whose maximum concentrations are mainly distributed between 60°N
596 and the equator, peaking concentrations of BC and OC as shown in Figs. 9 and 10 are located
597 near the tropics in the biomass burning regions (e.g., the maritime continent, Central Africa,
598 South America), and their seasonal variations from DJF to JJA are evidently weaker than
599 those of sulfate except in South America. In boreal summer, there are centers of high values
600 in the industrial regions in the Northern Hemisphere mid-latitudes (i.e., East Asia, South Asia,
601 Europe, and North America). These main features of spatial and seasonal variations in CMIP5
602 data are well captured by BCC-ESM1, and the BCC-ESM1 vs. CMIP5 spatial correlation
603 coefficients (Figure 13) are 0.90 (OC in DJF), 0.91 (BC in DJF), 0.91 (OC in JJA) and 0.92
604 (BC in JJA). There are less deviations of spatial pattern for OC in DJF and JJA, but larger
605 deviation for BC from CMIP5 data (Figure 13).

606 As shown in Figure 11, dust concentrations in the atmosphere show largest values over
607 strong source regions such as Northern Africa, Southwest and Central Asia, and Australia,
608 and over their outflow regions such as the Atlantic and the western Pacific. In DJF, the
609 CMIP5 data shows centers of high concentrations over East Asia and Central North America,
610 but both centers are missing in BCC-ESM1. However, these two high-value centers in the
611 CMIP5 data may not be true, since frozen soils in these areas in winter lead to unfavorable
612 conditions for soil erosion by winds. The spatial correlation coefficients between CMIP5 and
613 BCC-ESM1 remain high: 0.95 in JJA and 0.88 in DJF (Figure 13). Small deviations of spatial
614 pattern for dust simulations in BCC-ESM1 show less magnitude of dust maximums against
615 with CMIP5 data (Figure 13).

616 As shown in Figure 12, high sea salt concentrations are generally over the storm track

617 regions over the oceans, e.g., mid-latitudes in the Northern Oceans in DJF and the Southern
618 Ocean in JJA where wind speeds and thus sea salt emissions are higher. In addition, there is a
619 belt of high sea salt concentrations in the subtropics of both hemispheres where precipitation
620 scavenging is weak. Their spatial distributions in BCC-ESM1 are consistent with the CMIP5
621 data with correlation coefficients of 0.92 in JJA and 0.90 in DJF (Figure 13). The spatial
622 deviations of sea salt are much closer to CMIP5 data than those of sulfate, OC, BC, and dust
623 distributions (Figure 13).

624 Figure 14 shows vertical distributions of zonally-averaged annual mean concentrations
625 of sulfate, organic carbon, black carbon, dust, and sea salt aerosols in the period of 1991-2000.
626 Both BCC-ESM1 and CMIP5 results show that strong sulfur, OC, and BC emissions in the
627 industrial regions of the Northern Hemisphere mid-latitudes can rise upward and be
628 transported towards the North Pole in the mid- to upper troposphere. Most of OC, BC, and
629 dust aerosols are confined below 500 hPa, while sulfate can be transported to higher altitudes.
630 Sea salt aerosols are mostly confined below 700 hPa, as the particles are large in size and
631 favorable for wet removal and gravitational settling towards the surface. It can be seen that
632 BCC-ESM1 tends to simulate less upward transport of aerosols than the CMIP5 data, likely
633 reflecting the omission of deep convection transport of tracers in BCC-ESM1.

634 The CMIP5 data used here are mainly from model simulations. We will further evaluate
635 the BCC-ESM1 model results with ground observations. Annual mean SO_4^{2-} , BC and OC
636 aerosol observations from the Interagency Monitoring of Protected Visual Environments
637 (IMPROVE) sites over 1990-2005 in the United States
638 (<http://vista.cira.colostate.edu/IMPROVE/>) and from the European Monitoring and Evaluation
639 Programme (EMEP) (<http://www.emep.int>) sites over 1995-2005 are used. As shown in
640 Figure 15a and 15b, the BCC-ESM simulated sulfate concentrations are in general
641 comparable to the EMEP observations in Europe, but are systematically by about $1 \mu\text{g m}^{-3}$
642 higher than the U.S. IMPROVE observations. As for BC, there are large model biases at both
643 European and U.S. sites (Figs. 15c and 15d), especially BCC-ESM overestimates BC
644 concentrations at the IMPROVE sites. The observed OC concentrations are slightly
645 overestimated for IMPROVE sites but systematically underestimated for EMEP sites. Some
646 statistical features for simulated concentrations versus EMEP and IMPROVE observations are

647 listed in Table 7. These comparisons are overall fairly reasonable considering the
648 uncertainties in emissions and the coarse model resolution.

649 We then evaluate the simulated BC concentrations from BCC-ESM1 with the HIAPER
650 (High-Performance Instrumented Airborne Platform for Environmental Research)
651 Pole-to-Pole Observations (HIPPO) (Wofsy et al., 2011). The HIPPO campaign provided
652 observations of black carbon concentration profiles over Pacific Ocean and North America
653 between 2009 and 2011. Following Tilmes et al. (2016), model results here are sampled along
654 the HIPPO flight tracks and then averaged to different latitude and altitude bands for
655 comparison. As shown in Figure 16, BCC-ESM1 and HIPPO aircraft observations shows
656 reasonable agreement in terms of the spatial distributions and seasonal variations of BC levels.
657 BCC-ESM1 generally reproduces the observed hemispheric gradients of BC, i.e. the larger
658 burden in the NH compared to the SH, in consistent with Figures 10 and 14. The mean value
659 of modelled results along the flight track is 11.1 ng/kg, comparable to 8.2 ng/kg of the HIPPO
660 observations. The model shows large overestimations of BC observations over the tropics,
661 which is also found in the CAM4-chem global chemical model (Tilmes et al., 2016).

662 **4.4 Aerosol Optical Properties**

663 Aerosol optical depth (AOD) is an indicator of the reduction in incoming solar
664 radiation (at a particular wavelength) due to scattering and absorption of sunlight by aerosols.
665 In this study, we calculate the AOD at 550 nm for all aerosols including sulfate, BC, organic
666 carbon, sea salt and dust as the product of aerosol dry mass concentrations, aerosol water
667 content, and their specific extinction coefficients. The total AOD is calculated by summing
668 the AOD in each model layer for each aerosol species using the assumption that they are
669 externally mixed. The AOD observations retrieved from MODIS and MISR over the period of
670 1997-2003, and from AERONET over the period of 1998–2005 (<http://aeronet.gsfc.nasa.gov>)
671 are used to evaluate the averaged AOD at 550 nm in BCC-ESM. Figure 17 shows averages of
672 MISR and MODIS AOD with corresponding averages from BCC-ESM. The BCC-ESM1
673 simulated AOD generally captures the spatial distribution of MISR and MODIS retrievals.
674 The model overestimates AOD over East China. It also systematically underestimates the
675 MODIS observations in the Southern Hemisphere, but is closer to MISR observations. Figure

676 18 shows multi-years annual means of BCC-ESM1 simulated AOD values versus
677 observations from AERONET over the period of 1998–2005. The basic pattern of modeled
678 global AOD is similar to that of observations and their spatial correlation reaches 0.56. Large
679 values of AOD are mainly distributed in land continents such as North African, South Asia,
680 East Asia, Europe, and eastern part of North America. Figures 19a-19d present scatter plots of
681 observed versus simulated multi-year monthly mean AOD at those sites of AERONET in
682 Europe, North America, East Asia, and South Asia over the period of 1998-2005, respectively.
683 Model simulated monthly AOD generally agrees with observations within a factor of 2 for
684 most sites. BCC-ESM slightly overestimates the AOD in European and North American sites.
685 In those regions, BCC-ESM also slightly overestimates MODIS and MISR AOD observations
686 (Fig. 17).

687 **5. Summary and discussions**

688 This paper presents a primary evaluation of aerosols simulated in version 1 of the Beijing
689 Climate Center Earth System Model (BCC-ESM1) with the implementation of the interactive
690 atmospheric chemistry and aerosol based on the newly developed BCC-CSM2. Global
691 aerosols (including sulfate, organic carbon, black carbon, dust and sea salt) and major
692 greenhouse gases (e.g., O₃, CH₄, N₂O) in the atmosphere can be interactively simulated when
693 anthropogenic emissions are provided to the model. Concentrations of all aerosols in
694 BCC-ESM1 are determined by the processes of advective transport, emission, gas-phase
695 chemical reactions, dry deposition, gravitational settling, and wet scavenging by clouds and
696 precipitation. The nucleation and coagulation of aerosols are ignored in the present version of
697 BCC-ESM1. Effects of aerosols on radiation, cloud, and precipitation are fully included.

698 We evaluate the performance of BCC-ESM1 in simulating aerosols and their optical
699 properties in the 20th century following CMIP6 historical simulation according to the
700 requirement of the AerChemMIP. It is forced with anthropogenic emissions evolving from
701 1850 to 2014 but some WMGHGs such as CH₄, N₂O, CO₂, CFC11 and CFC12 are prescribed
702 using CMIP6 prescribed concentrations (to replace prognostic values of CH₄ and N₂O from
703 the chemistry scheme). Both direct and indirect effects of aerosols are considered in
704 BCC-ESM1. Initial conditions of the CMIP6 historical simulation are obtained from a
705 600-year piControl simulation in the absence of anthropogenic emissions, which well captures

706 the pre-industrial concentrations of SO_4^{2-} , organic carbon (OC), black carbon (BC), dust, and
707 sea salt aerosols and are consistent with the CMIP5 recommended concentrations for the year
708 1850. With the CMIP6 anthropogenic emissions of SO_2 , OC, and BC from 1850 to 2014 and
709 their natural emissions implemented in BCC-ESM1, the model simulated SO_4^{2-} , BC, and OC
710 aerosols in the atmosphere are highly correlated with the CMIP5-recommended data. The
711 long-term trends of CMIP5 aerosols from 1850 to 2000 are also well simulated by
712 BCC-ESM1. Global budgets of aerosols were evaluated through comparisons of BCC-ESM1
713 results for 1990-2000 with reports in various literatures for sulfate, BC, OC, sea salt, and dust.
714 Their annual total emissions, atmospheric mass loading, and mean lifetimes are all within the
715 range of values reported in relevant literature. Evaluations of the spatial and vertical
716 distributions of BCC-ESM1 simulated present-day SO_4^{2-} , OC, BC, Dust, and sea salt aerosol
717 concentrations against the CMIP5 datasets and in-situ measurements of surface networks
718 (IMPROVE in the U.S. and EMEP in Europe), and HIPPO aircraft observations indicate good
719 agreement among them. The BCC-ESM1 simulates weaker upward transport of aerosols from
720 the surface to the middle and upper troposphere (with reference to CMIP5-recommended
721 data), likely reflecting a lack of deep convection transport of chemical species in the present
722 version of BCC-ESM1. The AOD at 550 nm for all aerosols including sulfate, BC, OC, sea
723 salt, and dust aerosols was further compared with the satellite AOD observations retrieved
724 from MODIS and MISR and surface AOD observations from AERONET. The BCC-ESM1
725 model results are overall in good agreement with these observations within a factor of 2. All
726 these comparisons demonstrate the success of the implementation of interactive aerosol and
727 atmospheric chemistry in BCC-ESM1.

728 This work has only evaluated the ability of BCC-ESM1 to simulate aerosols. The
729 variations of aerosols especially for sulfate are related to other gaseous tracers such as OH
730 and NO_3 (Table 2), which are determined by the MOZART2 gaseous chemical scheme as
731 implemented in BCC-ESM1, and require further evaluation. As limited length of the text, the
732 other optical feature of aerosols such as extinction coefficients, single scattering albedo and
733 asymmetry parameters, and even their feedbacks on radiation and global temperature change
734 will be explored in the other paper. O_3 is evaluated in this work. Other GHGs such as CH_4 and

735 N₂O concentrations can be simulated when forced with emissions and their simulations also
736 need to be evaluated in future.

737 **6. Code and data availability**

738 The source codes of BCC-ESM1, model input files, and scripts to reproduce the
739 simulations that are presented in the article have been archived and made publicly available
740 for downloading from <https://zenodo.org/record/3609337> (Wu et al., 2020). Model output
741 data of BCC CMIP6 AerChemMIP simulations described in this paper are available on the
742 Earth System Grid Federation (ESGF)
743 ([https://cera-www.dkrz.de/WDCC/ui/cerasearch/cmip6?input=CMIP6.AerChemMIP.BCC.B](https://cera-www.dkrz.de/WDCC/ui/cerasearch/cmip6?input=CMIP6.AerChemMIP.BCC.BCC-ESM1)
744 [CC-ESM1, https://doi.org/10.22033/ESGF/CMIP6.1733](https://doi.org/10.22033/ESGF/CMIP6.1733); Zhang et al., 2019). Details about
745 ESGF are presented on the CMIP Panel website at
746 <http://www.wcrp-climate.org/index.php/wgcm-cmip/about-cmip>.

747

748 **Author contributions**

749 Tongwen Wu led the BCC-ESM1 development. All other co-authors have contributions
750 to it. Fang Zhang and Jie Zhang designed the experiments and carried them out. Tongwen Wu,
751 Laurent Li, Lin Zhang, Xiaohong Liu, Aixue Hu, and Jun Wang wrote the final document
752 with contributions from all other authors.

753

754 **Acknowledgements**

755 This work was supported by The National Key Research and Development Program of China
756 (2016YFA0602100). All the figures are created by the NCAR Command Language (Version
757 6.6.2) [Software].

758

759 **References**

760 Albani, S., Mahowald, N. M., Perry, A. T., Scanza, R. A., Zender, C. S., Heavens, N. G.,
761 Maggi, V., Kok, J. F., and Otto-Bliesner, B. L.: Improved dust representation in the
762 Community Atmosphere Model, *J. Adv. Model. Earth Syst.*, 6, 541–570,
763 doi:10.1002/2013MS000279, 2014.
764 Albrecht, B.: Aerosols, cloud microphysics, and fractional cloudiness, *Science*, 245, 1227–

765 1230, 1989.

766 Arora, V., Boer, G., Friedlingstein, P., Eby, M., Jones, C., Christian, J., Bonan, G., Bopp, L.,
767 Brovkin, V., Cadule, P., Hajima, T., Ilyina, T., Lindsay, K., Tjiputra, J., and Wu, T.:
768 Carbon-concentration and carbon-climate feedbacks in CMIP5 Earth system models. *J.*
769 *Climate*, 26, 5289–5314, 2013.

770 Austin, J., Butchart, N., and Shine, K. P.: Possibility of an Arctic ozone hole in a
771 doubled-CO₂ climate, *Nature*, 360, 221–225, 1992

772 Barth, M.C., Rasch, P.J., Kiehl, J.T., Benkowitz, C.M., and Schwartz, S.E.: Sulfur chemistry
773 in the National Center for Atmospheric Research Community Climate Model:
774 Description, evaluation, features, and sensitivity to aqueous chemistry. *J. Geophys. Res.*,
775 105, D1, 1387-1415, 2000.

776 Bey I., Jacob, D. J., Yantosca, R. M., Logan, J. A., Field, B., Fiore, A. M., Li, Q., Liu, H.,
777 Mickley, L. J., and Schultz, M.: Global modeling of tropospheric chemistry with
778 assimilated meteorology: Model description and evaluation, *J. Geophys. Res.*, 106,
779 23,073-23,096, 2001

780 Boucher, O., Lohmann, U.: The sulphate-CCN-cloud albedo effect – a sensitivity study with
781 two general circulation models, *Tellus 47B*, 281–300, 1995.

782 Brasseur, G. P., Hauglustaine, D. A., Walters, S., Rasch, P. J., Müller, J.-F., Granier, C., and
783 Tie, X. X.: MOZART, a global chemical transport model for ozone and related chemical
784 tracers: I. Model description, *J. Geophys. Res.*, 103, 28,265– 28,289, 1998.

785 Brasseur, G. P., Tie, X. X., Rasch, P. J., and Lefèvre, F.: A three - dimensional simulation of
786 the Antarctic ozone hole: Impact of anthropogenic chlorine on the lower stratosphere and
787 upper troposphere, *J. Geophys. Res.*, 102, 8909–8930, 1997.

788 Cariolle, D., Lasserre-Bigorry, A., and Royer, J.-F.: A general circulation model simulation of
789 the springtime Antarctic ozone decrease and its impact on midlatitudes, *J. Geophys. Res.*,
790 95, 1883–1898, 1990.

791 Cess, R. D.: Nuclear war: Illustrative effects of atmospheric smoke and dust upon solar
792 radiation, *Clim. Change*, 7, 237–251, 1985.

793 Chen, C., and Cotton, W. R.: The physics of the marine stratocumulus-capped mixed layer, *J.*
794 *Atmos. Sci.*, 44 (50), 2951–2977, 1987.

795 Chin, M., Ginoux, P., Kinne, S., Torres, O., Holben, B.N., Duncan, B.N., Martin, R.V., Logan, J.A.,
796 Higurashi, A., Naka-jima, T.: Tropospheric aerosol optical thickness from the GOCART

797 model and comparisons with satellite and Sun photometer measurements. *J. Atmos.*
798 *Sci.* 59:461–483, 2002.

799 Chuang, C. C., Penner, J. E., Taylor, K. E., Grossman, A. S., and Walton, J. J.: An assessment
800 of the radiative effects of anthropogenic sulfate, *J. Geophys. Res.*, 102, 3761–3778,
801 1997.

802 Collins, W. J., Lamarque, J.-F., Schulz, M., Boucher, O., Eyring, V., Hegglin, M. I.,
803 Maycock, A., Myhre, G., Prather, M., Shindell, D., Smith, S. J.: AerChemMIP:
804 quantifying the effects of chemistry and aerosols in CMIP6, *Geosci. Model Dev.*, 10,
805 585–607, 2017.

806 Collins, W. D., Rasch, P. J., Boville, B. A., Hack, J. J., McCaa, J. R., Williamson, D. L.,
807 Kiehl, J. T., Briegleb, B. P., Bitz, C., Lin, S.-J., Zhang, M., and Dai, Y.: Description of
808 the NCAR Community Atmosphere Model (CAM3). *Nat. Cent. for Atmos. Res.*,
809 Boulder, Colo., 2004.

810 Cooke, W.F., Wilson, J.J.N.: A global black carbon aerosol model. *J. Geophys. Res. Atmos.*
811 101, 19395–19409, 1996.

812 Cunnold, D., Alyea, F., Phillips, N., Prinn, R.: A three-dimensional dynamical-chemical
813 model of atmospheric ozone, *J. Atmos. Sci.*, 32, 170-194, 1975.

814 Dentener, F., Kinne, S., Bond, T., Boucher, O., Cofala, J., Generoso, S., Ginoux, P., Gong, S.,
815 Hoelzemann, J. J., Ito, A., Marelli, L., Penner, J. E., Putaud, J.-P., Textor, C., Schulz, M.,
816 van der Werf, G. R., and Wilson, J.: Emissions of primary aerosol and precursor gases in
817 the years 2000 and 1750 prescribed data-sets for AeroCom, *Atmos. Chem. Phys.*, 6,
818 4321–4344, doi:10.5194/acp-6-4321-2006, 2006.

819 Eyring, V., Bony, S., Meehl, G. A., Senior, C. A., Stevens, B., Stouffer, R. J., and Taylor, K.
820 E.: Overview of the Coupled Model Intercomparison Project Phase 6 (CMIP6)
821 experimental design and organization, *Geosci. Model Dev.*, 9, 1937–1958,
822 doi:10.5194/gmd-9-1937-2016, 2016.

823 Feichter, J., Kjellstrom, E., Rodhe, H., Dentener, F., Lelieveld, J., Roelofs, G.-J.: Simulation
824 of the tropospheric sulfur cycle in a global climate model, 30: 1693-1707, 1996.

825 Feng, L., Smith, S. J., Braun, C., Crippa, M., Gidden, M. J., Hoesly, R., Klimont, Z., van
826 Marle, M., van den Berg, M., and van der Werf, G. R.: Gridded Emissions for CMIP6,
827 *Geosci. Model Dev. Discuss.*, <https://doi.org/10.5194/gmd-2019-195>, 2019

828 Ghan, S. J. and Easter, R. C.: Impact of cloud-borne aerosol representation on aerosol direct

829 and indirect effects, *Atmos. Chem. Phys.*, 6, 4163–4174, 2006.

830 Ginoux, P., M. Chin, I. Tegen, J. M. Prospero, B. Holben, O. Dubovik, and S.-J. Lin (2001),
831 Sources and distributions of dust aerosols simulated with the GOCART model, *J.*
832 *Geophys. Res.*, 106, 20,255 – 20,274.

833 Giorgi, F., and Chameides, W. L.: The rainout parameterization in a photochemical model, *J.*
834 *Geophys. Res.*, 90, 7872–7880, 1985.

835 Guenther, A. B., Jiang, X., Heald, C. L., et al.: The Model of Emissions of Gases and
836 Aerosols from Nature Version 2.1 (MEGAN2.1): An Extended and Updated Framework
837 for Modeling Biogenic Emissions. *Geoscientific Model Development* 5(6): 1471–1492,
838 2012.

839 Guenther, A., Baugh, B. Brasseur, G., Greenberg, J., Harley, P., Klinger, L., Serca, D., and
840 Vierling, L.: Isoprene emission estimates and uncertainties for the Central African
841 EXPRESSO study domain, *J. Geophys. Res.*, 104(D23), 30, 625–630, 639, 1999.

842 Hess, M., Koepke, P., Schult, I.: Optical properties of aerosols and clouds: the software
843 package OPAC, *Bull. Am. Meteorol. Soc.*, 79, 831–844, 1998.

844 Hoesly, R. M., Smith, S. ., Feng, L., Klimont, Z., Janssens-Maenhout, G., Pitkanen, T.,
845 Seibert, J. J., Vu, L., Andres, R. J., Bolt, R. M., Bond, T. C., Dawidowski, L., Kholod, N.,
846 Kurokawa, J., Li, M., Liu, L., Lu, Z., Moura, M. C. P., O’Rourke, R. R., and Zhang Q.:
847 Historical (1750–2014) anthropogenic emissions of reactive gases and aerosols from the
848 Community Emission Data System (CEDS), *Geosci. Model Dev.*, 11, 369-408, 2018

849 Horowitz, L.W., Walters, S., Mauzerall, D. L., Emmons, L. K., Rasch, P. J., Granier, C., Tie,
850 X., Lamarque, J.-F., Schultz, M. G., Tyndall, G. S., Orlando, J. J., Brasseur, G. P.: A
851 global simulation of tropospheric ozone and related tracers: Description and evaluation
852 of MOZART, version 2, *J. Geophys. Res.*, 108(D24), 4784, doi:10.1029/2002JD002853,
853 2003.

854 Horowitz, L. W.: Past, present, and future concentrations of tropospheric ozone and aerosols:
855 Methodology, ozone evaluation, and sensitivity to aerosol wet removal, *J. Geophys. Res.*,
856 111, D22211, doi:10.1029/2005JD006937, 2006.

857 Hoffman, F. M., Randerson, J. T., Arora, V. K., Bao, Q., Cadule, P., Ji, D., Jones, C. D.,
858 Kawamiya, M., Khatiwala, S., Lindsay, K., Obata, A., Shevliakova, E., Six, K. D.,
859 Tjiputra, J. F., Volodin, E. M., and Wu, T.: Causes and implications of persistent
860 atmospheric carbon dioxide biases in Earth System Models, *J. Geophys. Res. Biogeosci.*,

861 119, 141–162, doi:10.1002/2013JG002381, 2014.

862 Holtslag, A. A. M., and Boville, B. A.: Local versus nonlocal boundary-layer diffusion in a
863 global climate model, *J. Climate*, 6, 1825–1842, 1993.

864 Hurtt, G.C., Chini, L.P., Frohking, S. et al.: Harmonization of land-use scenarios for the period
865 1500–2100: 600 years of global gridded annual land-use transitions, wood harvest, and
866 resulting secondary lands, *Climatic Change*, 109, 117-161, 2011.

867 Hurtt, G., et al.: input4MIPs.UofMD.landState.CMIP.UofMD-landState-2-1-h, version
868 20170126, Earth Syst. Grid Fed., <http://doi.org/10.22033/ESGF/input4MIPs.1127>, 2017.

869 Jacobson, M.Z.: Investigating cloud absorption effects: global absorption properties of black
870 carbon, tar balls, and soil dust in clouds and aerosols. *J. Geophys. Res.* 117, D06205,
871 2012.

872 Jones, C.D., Arora, V., Friedlingstein, P., Bopp, L., Brovkin, V., Dunne, J., Graven, H.,
873 Hoffman, F., Ilyina, T., John, J. G., Jung, M., Kawamiya, M., Koven, C., Pongratz, J.,
874 Raddatz, T., Randerson, J. T., and Zaehle, S.: C4MIP – The Coupled Climate–Carbon
875 Cycle Model Intercomparison Project: experimental protocol for CMIP6, *Geosci. Model*
876 *Dev.*, 9, 2853–2880, doi:10.5194/gmd-9-2853-2016, 2016.

877 Lamarque, J.-F., Shindell, D. T., Josse, B., Young, P. J., Cionni, I., Eyring, V., Bergmann, D.,
878 Cameron-Smith, P., Collins, W. J., Doherty, R., Dalsoren, S., Faluvegi, G., Folberth, G.,
879 Ghan, S. J., Horowitz, L. W., Lee, Y. H., MacKenzie, I. A., Nagashima, T., Naik, V.,
880 Plummer, D., Righi, M., Rumbold, S. T., Schulz, M., Skeie, R. B., Stevenson, D. S.,
881 Strode, S., Sudo, K., Szopa, S., Voulgarakis, A., and Zeng, G.: The Atmospheric
882 Chemistry and Climate Model Intercomparison Project (ACCMIP): overview and
883 description of models, simulations and climate diagnostics, *Geosci. Model Dev.*, 6, 179–
884 206, doi:10.5194/gmd-6-179-2013, 2013.

885 Lamarque, J.-F., Emmons, L. K., Hess, P. G., Kinnison, D. E., Tilmes, S., Vitt, F., Heald, C.
886 L., Holland, E. A., Lauritzen, P. H., Neu, J., Orlando, J. J., Rasch, P. J., and Tyndall, G.
887 K.: CAM-chem: description and evaluation of interactive atmospheric chemistry in the
888 Community Earth System Model, *Geosci. Model Dev.*, 5, 369–411, 2012

889 Lamarque, J.-F., Bond, T. C., Eyring, V., Granier, C., Heil, A., Klimont, Z., Lee, D., Liousse,
890 C., Mieville, A., Owen, B., Schultz, M. G., Shindell, D., Smith, S. J., Stehfest, E., Van
891 Aardenne, J., Cooper, O. R., Kainuma, M., Mahowald, N., McConnell, J. R., Naik, V.,
892 Riahi, K., and van Vuuren, D. P.: Historical (1850–2000) gridded anthropogenic and

893 biomass burning emissions of reactive gases and aerosols: methodology and application,
894 *Atmos. Chem. Phys.*, 10, 7017-7039, <https://doi.org/10.5194/acp-10-7017-2010>, 2010.

895 Lawrence, D. M., Hurtt, G. C., Arneeth, A., Brovkin, V., Calvin, K. V., Jones, A. D., Jones, C.
896 D., Lawrence, P. J., de Noblet-Ducoudré N., Pongratz, J., Seneviratne, S. I., and
897 Shevliakova, E.: The Land Use Model Intercomparison Project (LUMIP) contribution to
898 CMIP6: rationale and experimental design, *Geosci. Model Dev.*, 9, 2973–2998,
899 <https://doi.org/10.5194/gmd-9-2973-2016>, 2016.

900 Lohmann, U., Feichter, J., Penner, J. E., and Leaitch, W. R.: Indirect effect of sulfate and
901 carbonaceous aerosols: A mechanistic treatment. *J. Geophys. Res.*, 105, 12193–12206,
902 2000

903 Li, W., Zhang, Y., Shi, X., Zhou, W., Huang, A., Mu, M., Qiu, B., Ji, J.: Development of the
904 Land Surface Model BCC_AVIM2.0 and Its Preliminary Performance in
905 LS3MIP/CMIP6, *J. Meteor. Res.*, 33, 851-869, doi: 10.1007/s13351-019-9016-y, 2019.

906 Liu, X. H., Penner, J. E., and Herzog, M.: Global modeling of aerosol dynamics: Model
907 description, evaluation, and interactions between sulfate and nonsulfate aerosols, *J.*
908 *Geophys. Res.-Atmos.*, 110, D18206, doi:10.1029/2004jd005674, 2005.

909 Liu, X., Easter, R.C. Ghan, S.J., Zaveri, R., Rasch, P., Shi, X., Lamarque, J.-F., Gettelman, A.,
910 Morrison, H., Vitt, F., Conley, A., Park, S., Neale, R., Hannay, C., Ekman, A.M., Hess,
911 P., Mahowald, N., Collins, W., Iacono, M.J., Bretherton, C.S., Flanner, M.G., and
912 Mitchell, D.: Toward a Minimal Representation of Aerosols in Climate Models:
913 Description and Evaluation in the Community Atmosphere Model CAM5.
914 *Geos.Model.Dev.* 5(3):709-739. 2012.

915 Liu, X., Ma, P. -L., Wang, H., Tilmes, S., Singh, B., Easter, R. C., Ghan, S. J., and Rasch, P.
916 J.: Description and evaluation of a new four-mode version of the Modal Aerosol Module
917 (MAM4) within version 5.3 of the Community Atmosphere Model, *Geosci. Model Dev.*,
918 9, 505–522, <https://doi.org/10.5194/gmd-9-505-2016>, 2016.

919 Liu, J., Mauzerall, D.L., Horowitz, L.W., Ginoux, P., Fiore, A.M.: Evaluation intercontinental
920 transport of fine aerosols: (1) methodology, global aerosol distribution and optical depth.
921 *Atmos Environ* 43:4327–4338, 2009.

922 Lu, X., Zhang, L., Wu, T., Long, M., Wang, J., Jacob, D., Zhang F., Zhang, J., Eastham, S.,
923 Hu, L., Zhu, L., Liu, X., an Wei, M.: Development of the global atmospheric general
924 circulation-chemistry model BCC-GEOS-Chem v1.0: model description and evaluation,

925 submitted to Geos.Model.Dev.

926 Mahowald, N., Lamarque, J.-F., Tie, X., and Wolff, E.: Sea salt aerosol response to climate
927 change: last glacial maximum, preindustrial and doubled carbon dioxide climates, *J.*
928 *Geophys. Res.*, 111, D05303, doi:10.1029/2005JD006459, 2006.

929 Martin, R. V., et al.: Interpretation of TOMS observations of tropical tropospheric ozone with
930 a global model and in situ observations, *J. Geophys. Res.*, 107(D18), 4351,
931 doi:10.1029/2001JD001480, 2002.

932 Matsui, H., and Mahowald, N.: Development of a global aerosol model using a
933 two-dimensional sectional method: 2. Evaluation and sensitivity simulations, *J. Adv.*
934 *Model. Earth Syst.*, 9, 1887 – 1920, doi:10.1002/2017MS000937, 2017.

935 Matthes, K., Funke, B., Andersson, M. E., Barnard, L., Beer, J., Charbonneau, P., Clilverd, M.
936 A., Dudok de Wit, T., Haberreiter, M., Hendry, A., Jackman, C. H., Kretschmar, M.,
937 Kruschke, T., Kunze, M., Langematz, U., Marsh, D. R., Maycock, A. C., Misios, S.,
938 Rodger, C. J., Scaife, A. A., Seppälä, A., Shanguan, M., Sinnhuber, M., Tourpali, K.,
939 Usoskin, I., van de Kamp, M., Verronen, P. T., and Versick, S.: Solar forcing for CMIP6
940 (v3.2), *Geosci. Model Dev.*, 10, 2247–2302, <https://doi.org/10.5194/gmd-10-2247-2017>,
941 2017.

942 Meinshausen, M., Vogel, E., Nauels, A., Lorbacher, K., Meinshausen, N., Etheridge, D. M.,
943 Fraser, P. J., Montzka, S. A., Rayner, P. J., Trudinger, C. M., Krummel, P. B., Beyerle,
944 U., Canadell, J. G., Daniel, J. S., Enting, I. G., Law, R. M., Lunder, C. R., O'Doherty, S.,
945 Prinn, R. G., Reimann, S., Rubino, M., Velders, G. J. M., Vollmer, M. K., Wang, R. H. J.,
946 and Weiss, R.: Historical greenhouse gas concentrations for climate modelling (CMIP6),
947 *Geosci. Model Dev.*, 10, 2057–2116, <https://doi.org/10.5194/gmd-10-2057-2017>, 2017.

948 Mora, C., Wei, C.-L., Rollo, A., Amaro, T., Baco, A.R., Billett, D., Bopp, L., Chen, Q.,
949 Collier, M., Danovaro, R., Gooday, A.J., Grupe, B.M., Halloran, P.R., Ingels, J., Jones,
950 D.O.B., Levin, L.A., Nakano, H., Norling, K., Ramirez-Llodra, E., Rex, M., Ruh, H.A.,
951 Smith, C.R., Sweetman, A.K., Thurber, A.R., Tjiputra, J. F., Usseglio, P., Watling, L.,
952 Wu, T., Yasuhara, M.: Biotic and human vulnerability to projected ocean
953 biogeochemistry change over the 21st century, *PLoS Biol* 11(10): e1001682.
954 doi:10.1371/journal.pbio.1001682, 2013.

955 NCAR Command Language (Version 6.6.2) [Software], Boulder, Colorado:
956 UCAR/NCAR/CISL/TDD. <http://dx.doi.org/10.5065/D6WD3XH5>, 2019.

957 Neale, R. B., et al.: Description of the NCAR Community Atmosphere Model (CAM 4.0),
958 NCAR Tech. Note, TN-485, pp. 212, Natl. Cent. for Atmos. Res., Boulder, Colo., 2010

959 Neu, J. L. and Prather, M. J.: Toward a more physical representation of precipitation
960 scavenging in global chemistry models: cloud overlap and ice physics and their impact
961 on tropospheric ozone, *Atmos. Chem. Phys. Discuss.*, 11, 24413–24466,
962 doi:10.5194/acpd-11-24413-2011, 2011.

963 Olivier, J.G.J., Bouwman, A.F., Van der Maas, C.W.M., Berdowski, J.J.M., Veldt, C., Bloos,
964 J.P.J., Visschedijk, A.J.H., Zandveld, P.Y.J., Haverslag, J.L., Description of EDGAR
965 Version 2.0: A set of global emission inventories of greenhouse gases and ozone
966 depleting substances for all anthropogenic and most natural sources on a per country
967 basis and on 1° x 1° grid. RIVM Techn. Report nr. 771060002, TNO-MEP report nr.
968 R96/119. Nat. Inst. Of Public Health and the Environment/ Netherlands Organisation for
969 Applied Scientific Research, Bilthoven, 1996.

970 Peng, Y., and Lohmann, U.: Sensitivity study of the spectral dispersion of the cloud droplet
971 size distribution on the indirect aerosol effect, *Geophys. Res. Lett.*, 30(10), 1507,
972 doi:10.1029/2003GL017192, 2003.

973 Price, C., and Rind, D.: A simple lightning parameterization for calculating global lightning
974 distributions, *J. Geophys. Res.*, 97, 9919-9933, 1992.

975 Quaas, J., Boucher, O., and Lohmann, U.: Constraining the total aerosol indirect effect in
976 the LMDZ and ECHAM4 GCMs using MODIS satellite data. *Atmos Chem Phys* 6,947–
977 955, 2006.

978 Sander, S., Friedl, R. R., Ravishankara, A. R., et al.: Chemical Kinetics and Photochemical
979 Data for Use in Atmospheric Studies, Evaluation Number 14, JPL Publication 02-25,
980 NASA, Jet Propulsion Laboratory, California Institute of Technology, Pasadena, CA,
981 2003.

982 Schlesinger, M. E., Mintz, Y.: Numerical simulation of ozone production, transport and
983 distribution with a global atmospheric general circulation model, *J. Atmos. Sci.*, 36:
984 1325-1361, 1979.

985 Shindell, D.T., Horowitz, L.W., Schwarzkopf, M.D.: Composition Models in Climate
986 Projections Based on Emissions Scenarios for Long-Lived and Short-Lived Radiatively
987 Active Gases and Aerosols. H. Levy II, D.T. Shindell, A. Gilliland, M.D. Schwarzkopf,

988 L.W.Horowitz, (eds.) .A Report by the U.S.Climate Change Science Program and the
989 Subcommittee on Global Change Research, Washington, D.C., 2008

990 Solomon, S.: Stratospheric ozone depletion: A review of concepts and history, *Reviews of*
991 *Geophysics*, 37, 275–316, 1999.

992 Taylor, K.E., Stouffer, R. J., Meehl, G. A.: An overview of CMIP5 and the experiment design,
993 *Bull. Am. Meteorol. Soc.* 93, 485-498, 2012.

994 Tegen, I., Neubauer, D., Ferrachat, S., Siegenthaler-Le Drian, C., Bey, I., Schutgens, N., Stier,
995 P., Watson-Parris, D., Stanelle, T., Schmidt, H., Rast, S., Kokkola, H., Schultz, M.,
996 Schroeder, S., Daskalakis, N., Barthel, S., Heinold, B., and Lohmann, U.: The global
997 aerosol–climate model ECHAM6.3–HAM2.3 – Part 1: Aerosol evaluation, *Geosci.*
998 *Model Dev.*, 12, 1643–1677, <https://doi.org/10.5194/gmd-12-1643-2019>, 2019.

999 Textor, C., Schulz, M., Guibert, S., Kinne, S., Balkanski, Y., Bauer, S., Berntsen, T., Berglen,
1000 T., Boucher, O., Chin, M., Dentener, F., Diehl, T., Easter, R., Feichter, H., Fillmore, D.,
1001 Ghan, S., Ginoux, P., Gong, S., Grini, A., Hendricks, J., Horowitz, L., Huang, P., Isaksen,
1002 I., Iversen, I., Kloster, S., Koch, D., Kirkevåg, A., Kristjansson, J. E., Krol, M., Lauer, A.,
1003 Lamarque, J. F., Liu, X., Montanaro, V., Myhre, G., Penner, J., Pitari, G., Reddy, S.,
1004 Seland, Ø., Stier, P., Takemura, T., and Tie, X.: Analysis and quantification of the
1005 diversities of aerosol life cycles within AeroCom, *Atmos. Chem. Phys.*, 6, 1777–1813,
1006 <https://doi.org/10.5194/acp-6-1777-2006>, 2006.

1007 Thomason, L. W., Ernest, N., Millán, L., Rieger, L., Bourassa, A., Vernier, J. P., Manney, G.,
1008 Luo, B.P., Arfeuille, F., Peter, T.: A global space - based stratospheric aerosol
1009 climatology: 1979-2016. *Earth System Science Data*, 10(1), 469–492, doi:
1010 [10.5194/essd-10-469-2018](https://doi.org/10.5194/essd-10-469-2018), 2018.

1011 Tie, X., Brasseur, G., Emmons, L., Horowitz, L., and Kinnison, D.: Effects of aerosols on
1012 tropospheric oxidants: A global model study, *J. Geophys. Res.*, 106, 2931– 2964, 2001.

1013 Tie, X., Madronich, S., Walters, S., Edwards, D., Ginoux, P., Mahowald, N., Zhang, R., Luo,
1014 C., and Brasseur, G.: Assessment of the global impact of aerosols on tropospheric
1015 oxidants, *J. Geophys. Res.*, 110, D03204, doi:10.1029/2004JD005359, 2005.

1016 Tilmes, S., Lamarque, J.-F., Emmons, L. K., Kinnison, D. E., Marsh, D., Garcia, R. R., Smith,
1017 A. K., Neely, R. R., Conley, A., Vitt, F., Val Martin, M., Tanimoto, H., Simpson, I.,
1018 Blake, D. R., and Blake, N.: Representation of the Community Earth System Model
1019 (CESM1) CAM4-chem within the Chemistry-Climate Model Initiative (CCMI),

1020 Geoscientific Model Development, 9, 1853-1890, 2016.

1021 Todd-Brown, K.E.O., Randerson, J.T., Hopkins, F., Arora, V., Hajima, T., Jones, C.,
1022 Shevliakova, E., Tjiputra, J., Volodin, E., Wu, T., Zhang, Q., Allison, S.D.: Changes in
1023 soil organic carbon storage predicted by Earth system models during the 21st century,
1024 Biogeosciences, 11, 2341-2356, 2014.

1025 Van Marle, M.J.E., S. Kloster, B.I. Magi, J.R. Marlon, A.-L. Daniau, R.D. Field, A. Arneth,
1026 M. Forrest, S. Hantson, N.M. Kehrwald, W. Knorr, G. Lasslop, F. Li, S. Mangeon, C.
1027 Yue, J.W. Kaiser, and G.R. van der Werf, 2017: Historic global biomass burning
1028 emissions for CMIP6 (BB4CMIP) based on merging satellite observations with proxies
1029 and fire models (1750-2015). Geosci. Model Dev., 10, 3329-3357,
1030 doi:10.5194/gmd-10-3329-2017.

1031 Wang, J., Hoffmann, A. A., Park, R., Jacob, D. J., and Martin, S. T.: Global distribution of
1032 solid and aqueous sulfate aerosols: effect of the hysteresis of particle phase transitions, J.
1033 Geophys. Res., 113, D11206, Doi:11210.11029/12007JD009367, 2008a.

1034 Wang, J., Jacob, D. J., and Martin, S. T.: Sensitivity of sulfate direct climate forcing to the
1035 hysteresis of particle phase transitions, J. Geophys. Res., 113, D11207,
1036 doi:11210.11029/12007JD009368, 2008b.

1037 Wesely, M. L.: Parameterization of surface resistance to gaseous dry deposition in
1038 regional-scale numerical models, Atmos. Environ., 23, 1293–1304, 1989.

1039 Wild, M., Folini, D., Schar, C., Loeb, N., Dutton, E.G., Konig-Langlo, G.: The global energy
1040 balance from a surface perspective, Climate Dynamics, 40: 3107-3134, 2013.

1041 Williamson, D. L., and Rasch, P. J.: Two-dimensional semi-Lagrangian transport with
1042 shapepreserving interpolation, Mon. Wea. Rev., 117, 102–129, 1989.

1043 Wofsy, S. C. and the HIPPO team: HIAPER Pole-to-Pole Observations (HIPPO): fine-grained,
1044 global-scale measurements of climatically important atmospheric gases and aerosols,
1045 Philo T. R. Soc. A, 369, 2073–86, doi:10.1098/rsta.2010.0313, 2011.

1046 Wu, T., Song, L., Li, W., Wang, Z., Zhang, H., Xin, X., Zhang, Y., Zhang, L., Li, J., Wu, F.,
1047 Liu, Y., Zhang, F., Shi, X., Chu, M., Zhang, J., Fang, Y., Wang, F., Lu, Y., Liu, X., Wei,
1048 M., Liu, Q., Zhou, W., Dong, M., Zhao, Q., Ji, J., Li, L., Zhou, M.: An overview of BCC
1049 climate system model development and application for climate change studies. J. Meteor.
1050 Res., 28(1), 34-56, 2014.

1051 Wu, T., Li, W., Ji, J., Xin, X., Li, L., Wang, Z, Zhang, Y., Li, J., Zhang, F., Wei, M., Shi, X.,

1052 Wu, F., Zhang, L., Chu, M., Jie, W., Liu, Y., Wang, F., Liu, X., Li, Q., Dong, M., Liang,
1053 X., Gao, Y., Zhang, J.: Global carbon budgets simulated by the Beijing climate center
1054 climate system model for the last century. *J Geophys Res Atmos*, 118, 4326-4347. doi:
1055 10.1002/jgrd.50320, 2013.

1056 Wu, T., Lu, Y., Fang, Y., Xin, X., Li, L., Li, W., Jie, W., Zhang, J., Liu, Y., Zhang, L., Zhang,
1057 F., Zhang, Y., Wu, F., Li, J., Chu, M., Wang, Z., Shi, X., Liu, X., Wei, M., Huang, A.,
1058 Zhang, Y., and Liu, X.: The Beijing Climate Center Climate System Model (BCC-CSM):
1059 the main progress from CMIP5 to CMIP6, *Geos.Model Dev.*, 12, 1573-1600,
1060 <http://doi.org/10.5194/gmd-12-1573-2019>, 2019.

1061 Wu, Tongwen, Zhang, Fang, Zhang, Jie, et al.: Model code and data for Wu et al, "Beijing
1062 Climate Center Earth System Model version 1 (BCC-ESM1): Model Description and
1063 Evaluation of Aerosol Simulations", GMD publication.
1064 <http://doi.org/10.5281/zenodo.3609337>, 2020.

1065 Young, P. J., Archibald, A. T., Bowman, K. W., Lamarque, J. F., Naik, V., Stevenson, D. S.,
1066 Tilmes, S., Voulgarakis, A., Wild, O., Bergmann, D., Cameron-Smith, P., Cionni, I.,
1067 Collins, W. J., Dalsøren, S. B., Doherty, R. M., Eyring, V., Faluvegi, G., Horowitz, L.
1068 W., Josse, B., Lee, Y. H., MacKenzie, I. A., Nagashima, T., Plummer, D. A., Righi, M.,
1069 Rumbold, S. T., Skeie, R. B., Shindell, D. T., Strode, S. A., Sudo, K., Szopa, S., and
1070 Zeng, G.: Pre-industrial to end 21st century projections of tropospheric ozone from the
1071 Atmospheric Chemistry and Climate Model Intercomparison Project (ACCMIP), *Atmos.*
1072 *Chem. Phys.*, 13, 2063-2090, <http://doi.org/10.5194/acp-13-2063-2013>, 2013.

1073 Young, P. J., Naik, V., Fiore, A. M., Gaudel, A., Guo, J., Lin, M. Y., Neu, J. L., Parrish, D. D.,
1074 Rieder, H. E., Schnell, J. L., Tilmes, S., Wild, O., Zhang, L., Ziemke, J. R., Brandt, J.,
1075 Delcloo, A., Doherty, R. M., Geels, C., Hegglin, M. I., Hu, L., Im, U., Kumar, R., Luhar,
1076 A., Murray, L., Plummer, D., Rodriguez, J., Saiz-Lopez, A., Schultz, M. G., Woodhouse,
1077 M. T., and Zeng, G.: Tropospheric Ozone Assessment Report: Assessment of
1078 global-scale model performance for global and regional ozone distributions, variability,
1079 and trends, *Elem Sci Anth*, 6, 10, <http://doi.org/10.1525/elementa.265>, 2018.

1080 Zender, C., Bian, H., and Newman, D.: Mineral Dust Entrainment and Deposition (DEAD)
1081 model: Description and 1990s dust climatology, *J. Geophys. Res.*, 108(D14), 4416, doi:
1082 10.1029/2002JD002775, 2003.

1083 Zhang, J., Wu, T., Shi, X., Zhang F., Li, J., Chu, M., Liu, Q., Yan, J., Ma, Q., Wei, M.: BCC

1084 BCC-ESM1 model output prepared for CMIP6 AerChemMIP, Earth System Grid
1085 Federation, <https://doi.org/10.22033/ESGF/CMIP6.1733>, 2019.
1086

1087 Table 1. Chemical species considered in BCC-AGCM3-Chem. Species marked with star (*)
 1088 denote those added in BCC-ESM1 apart from the 63 species used in MOZART2. In the
 1089 column of surface emission, interactive surface emissions are considered for sea salt and dust.
 1090

Species	Dry deposition	Wet deposition	Surface emission	Aircraft emission	Volcanic emission
O ₃	✓				
N ₂ O			✓		
N					
NO	✓		✓	✓	
NO ₂	✓				
NO ₃					
HNO ₃	✓	✓			
HO ₂ NO ₂	✓	✓			
N ₂ O ₅					
CH ₄	✓		✓	✓	
CH ₃ O ₂					
CH ₃ OOH	✓	✓			
CH ₂ O	✓	✓	✓		
CO	✓		✓	✓	
OH					
HO ₂					
H ₂ O ₂	✓	✓			
C ₃ H ₆			✓		
ISOP			✓		
Gas tracers					
PO ₂					
CH ₃ CHO	✓	✓	✓		
POOH	✓	✓			
CH ₃ CO ₃					
CH ₃ COOOH	✓	✓			
PAN	✓				
ONIT	✓	✓			
C ₂ H ₆			✓		
C ₂ H ₄			✓		
C ₄ H ₁₀			✓		
MPAN	✓				
ISOPO ₂					
MVK		✓			
MACR		✓			
MACRO ₂					
MACROOH	✓	✓			
MCO ₃					
C ₂ H ₅ O ₂					
C ₂ H ₅ OOH	✓	✓			
C ₁₀ H ₁₆			✓		

1091

1092

Table 1. Continued.

Species name	Dry deposition	Wet deposition	Surface emission	Aircraft emission	Volcanic emission
C ₃ H ₈			✓		
C ₃ H ₇ O ₂					
C ₃ H ₇ OOH	✓	✓			
CH ₃ COCH ₃	✓		✓		
ROOH		✓			
CH ₃ OH	✓	✓	✓		
C ₂ H ₅ OH	✓	✓	✓		
GLYALD	✓	✓			
HYAC	✓	✓			
EO ₂					
EO					
HYDRALD	✓	✓			
RO ₂					
CH ₃ COCHO	✓	✓	✓		
Rn-222					
Pb-210	✓	✓			
ISOPNO ₃		✓			
ONITR	✓	✓			
XO ₂					
XOOH	✓	✓			
ISOPOOH	✓	✓			
H ₂	✓		✓		
Stratospheric O ₃	✓				
Inert O ₃	✓				
SO ₂ *	✓	✓	✓	✓	✓
DMS*			✓		
NH ₃ *			✓	✓	
SO ₄ ²⁻ *	✓	✓			
OC1*	✓	✓	✓	✓	
OC2*	✓	✓	✓	✓	
BC1*	✓	✓	✓	✓	
BC2*	✓	✓	✓	✓	
SSLT01*	✓	✓			
SSLT02*	✓	✓			
SSLT03*	✓	✓			
SSLT04*	✓	✓			
DST01*	✓	✓			
DST02*	✓	✓			
DST03*	✓	✓			
DST04*	✓	✓			

1096 Table 2. Gas-phase chemical reactions for NH₃ and bulk aerosols precursors following
 1097 CAM-Chem (Lamarque et al., 2012). The reaction rates (s⁻¹) refer to Tie et al. (2001) and
 1098 Sander et al. (2003), and Cooke and Wilson (1996). Temperature (T) is expressed in K, air
 1099 density (M) in molecule cm⁻³, ki and ko in cm³ molecule⁻¹ s⁻¹.
 1100

Chemical reactions	Rate
NH ₃ + OH → H ₂ O	1.70E-12*exp(-710/T)
SO ₂ + OH → SO ₄ ²⁻	ko/(1.+ko*M/ki)*f**(1./(1.+log10(ko*M/ki))), in which ko=3.0E-31*(300/T)**3.3; ki=1.E-12; f =0.6
DMS + OH → SO ₂	9.60E-12*exp(-234./T)
DMS + OH → .5*SO ₂ + .5*HO ₂	1.7E-42*exp(7810/T)*M*0.21/(1+5.5E-31*exp(7460/T)* M* 0.21)
DMS + NO ₃ → SO ₂ + HNO ₃	1.90E-13*exp(520/T)
BC1 → BC2	7.10E-06
OC1 → OC2	7.10E-06

1101
 1102

1103

1104

1105

Table 3. Size and density parameters of bulk aerosols.

Aerosols	Species Name	Mean radius (μm) / bin size (μm)	Geometric standard deviation (μm)	Density (g cm^{-3})
SO_4^{2-}	Sulfate	0.05	2.03	1.77
BC1	hydrophobic black carbon	0.02	2.00	1.0
BC2	hydrophilic black carbon	0.02	2.00	1.0
OC1	hydrophobic organic carbon	0.03	2.24	1.8
OC2	hydrophilic organic carbon	0.03	2.24	1.8
DST01	Dust	0.55 / bin: 0.1-1.0	2.00	2.5
DST02	Dust	1.75 / bin: 1.0-2.5	2.00	2.5
DST03	Dust	3.75 / bin: 2.5-5.0	2.00	2.5
DST04	Dust	7.50 / bin: 5.0-10.	2.00	2.5
SSLT01	Sea salt	0.52 / bin: 0.2-1.0	2.00	2.2
SSLT02	Sea salt	2.38 / bin: 1.0-3.0	2.00	2.2
SSLT03	Sea salt	4.86 / bin: 3.0-10.	2.00	2.2
SSLT04	Sea salt	15.14 / bin: 10.-20.	2.00	2.2

1106

Table 4. Source of emission data. MOZART2 data denote the standard tropospheric chemistry package for MOZART contains surface emissions from the EDGAR 2.0 data base (Olivier et al., 1996). ACCMIP data are downloaded from the IPCC ACCMIP emission inventory (<http://accent.aero.jussieu.fr/ACCMIP.php>) and they vary from 1850 to 2000, in 10-year steps (Lamarque et al., 2010). CMIP6 data are from <https://esgf-node.llnl.gov/search/input4mips/>. Anthropogenic emission includes Industrial and fossil fuel use, agriculture, ships, and etc. Biomass burning includes vegetation fires incl. fuel wood and agricultural burning.

Species	Anthropogenic emission	Biomass burning	Biogenic emissions from vegetation	Biogenic emissions from soil	Oceanic emissions	Airplane emission	Volcanic emission
C ₂ H ₄	CMIP6	CMIP6	On-line computation		MOZART2		
C ₂ H ₅ OH	CMIP6	CMIP6					
C ₂ H ₆	CMIP6	CMIP6	ACCMIP		MOZART2		
C ₃ H ₆	CMIP6	CMIP6	On-line computation		MOZART2		
C ₃ H ₈	CMIP6	CMIP6	ACCMIP		MOZART2		
C ₄ H ₁₀	CMIP6	CMIP5	MOZART2		MOZART2		
CH ₂ O	CMIP6	CMIP6					
CH ₃ CHO	ACCMIP	CMIP6					
CH ₃ COCHO		CMIP6					
CH ₃ OH	ACCMIP	CMIP6	ACCMIP				
CH ₃ COCH ₃	ACCMIP	ACCMIP	On-line computation		MOZART2		
ISOP		CMIP5	On-line computation				
C ₁₀ H ₁₆		CMIP6	On-line computation				
CH ₄	CMIP6	CMIP6	MOZART2		MOZART2	CMIP6	
CO	CMIP6	CMIP6	ACCMIP	MOZART2	ACCMIP	CMIP6	
H ₂	MOZART2	CMIP6		MOZART2	MOZART2		
N ₂ O	MOZART2	CMIP6		MOZART2	MOZART2		
NH ₃	CMIP6	CMIP6		ACCMIP	ACCMIP	CMIP6	
NO	CMIP6	CMIP6		ACCMIP		CMIP6	
SO ₂	CMIP6	CMIP6				CMIP6	ACCMIP
DMS					ACCMIP		
OC1	CMIP6	CMIP6				CMIP6	
OC2	CMIP6	CMIP6	On-line computation			CMIP6	
BC1	CMIP6	CMIP6				CMIP6	
BC2	CMIP6	CMIP6				CMIP6	

Table 5. Global budgets for DMS, SO₂, and sulfate in the period of 1991 to 2000. Units are sources and sinks, Tg(S) yr⁻¹; burden, Tg; lifetime, days.

		BCC-ESM (1991-2000 mean)	Other studies and CMIP5 data
DMS	Sources	27.4	
	Emission	27.4	10.7-23.7 ^a
	Sinks	28.0	
	Gas-phase oxidation	28.0	
	Burden	0.12	0.04-0.29 ^a
	Lifetime	0.78	0.5-3.0 ^a
SO ₂	Sources	76.93	
	Emission at surface	63.63	
	Emission from airplane	0.10	
	DMS oxidation	13.20	10.0-24.7 ^a
	Sinks	76.96	
	Dry deposition	18.53	16.0-55.0 ^a
	Wet deposition	9.36	0.0-19.9 ^a
	Gas-phase oxidation	10.33	6.1-16.8 ^a
	Aqueous-phase oxidation	38.74	24.5-57.8 ^a
Burden	0.48	0.40-1.22 ^a	
Lifetime	1.12	0.6-2.6 ^a	
SO ₄ ²⁻	Sources	49.05	59.67 ± 13.13 ^b
	Emission	0.00	
	SO ₂ aqueous-phase oxidation	38.73	
	SO ₂ gas-phase oxidation	10.32	
	Sinks	49.06	
	Dry deposition	2.20	4.96-5.51 ^d
	Wet deposition	46.86	39.34-40.20 ^d
	Burden	1.89	1.98 ± 0.48 ^b , 1.71 ^c , 1.2 ^g , 2.22-2.43 ^h
	Lifetime	4.69	4.12 ± 0.74 ^b , 3.72-3.77 ^d 3.3 ^g , 3.7-4.0 ^h

Notes: References denote a for Liu et al. (2005), b for Textor et al. (2006), c for the values derived from CMIP5 prescribed aerosol masses averaged from 1991 to 2000, d for Liu et al. (2012), g for Matsui and Mahowald (2017), and h for Tegen et al. (2019). Values of DMS, SO₂, and sulfate burdens in the literature d are transferred from TgS to Tg (species) for units consistence.

Table 6. Same as Table 5, but for global budgets for black carbon, organic carbon, dust, and sea salts. Units are sources and sinks, Tg yr⁻¹; burden, Tg; lifetime, days.

		BCC-ESM (1991-2000 mean)	Other studies and CMIP5 data
BC	Sources	7.22	
	Emission	7.22	11.9 ± 2.7 ^b , 7.8 ^g
	Sinks	7.24	7.75 ^d , 7.8 ^g
	Dry deposition	0.90	0.27 ^g , 1.30-1.64 ^e
	Wet deposition	6.34	7.5 ^g , 6.10-6.45 ^e
	Burden	0.13	0.114 ^c , 0.24 ± 0.1 ^b , 0.11 ^g , 0.14-0.26 ^h , 0.084-0.123 ^e
	Lifetime	6.60	7.12 ± 2.35 ^b , 3.95-4.80 ^e , 5.0 ^g , 6.3-7.5 ^h
OC	Sources	32.29	
	Fossil and biofuel emission	13.91	
	Natural emission	18.38	
	Sinks	32.30	
	Dry deposition	2.44	
	Wet deposition	29.86	
	Burden	0.62	0.69 ^c , 1.7 ± 0.45 ^b , 1.0-2.2 ^h
Lifetime	5.00	6.54 ± 1.76 ^b , 4.56-4.90 ^d , 6.4 ^g , 5.4-6.6 ^h	
Dust	Sources	2592.0	1840 ^b , 2943.5-3121.9 ^d , 2677 ^g
	Sinks	2592.0	
	Dry deposition	1630.8	1444 ^g
	Wet deposition	961.2	1245 ^g
	Burden	22.93	20.41 ^c , 22.4-24.7 ^d , 35.9 ^f , 19.2 ± 7.68 ^b , 28.5 ^g , 16.5-17.9 ^h
	Lifetime	3.23	4.14 ± 1.78 ^b , 2.61-3.07 ^d , 3.9 ^g , 5.3-5.7 ^h
Sea Salt	Sources	4667.2	4965.5-5004.1 ^d , 5039 ^g
	Sinks	4667.4	
	Dry deposition	2978.5	2158 ^g
	Wet deposition	1688.9	2918 ^g
	Burden	11.89	7.58-10.37 ^a , 6.4 ± 3.4 ^b , 11.84 ^c , 13.6 ^g , 3.9 ^h
	Lifetime	0.93	0.41 ± 0.24 ^b , 0.55-0.76 ^d , 0.98 ^g , 1.2-1.3 ^h

Notes: References denote a for Liu et al. (2005), b for Textor et al. (2006), c derived from CMIP5 prescribed aerosol masses averaged from 1991 to 2000, d for Liu et al. (2012), e for Liu et al. (2016), f for Ginoux (2001), g for Matsui and Mahowald (2017), and h for Tegen et al. (2019).

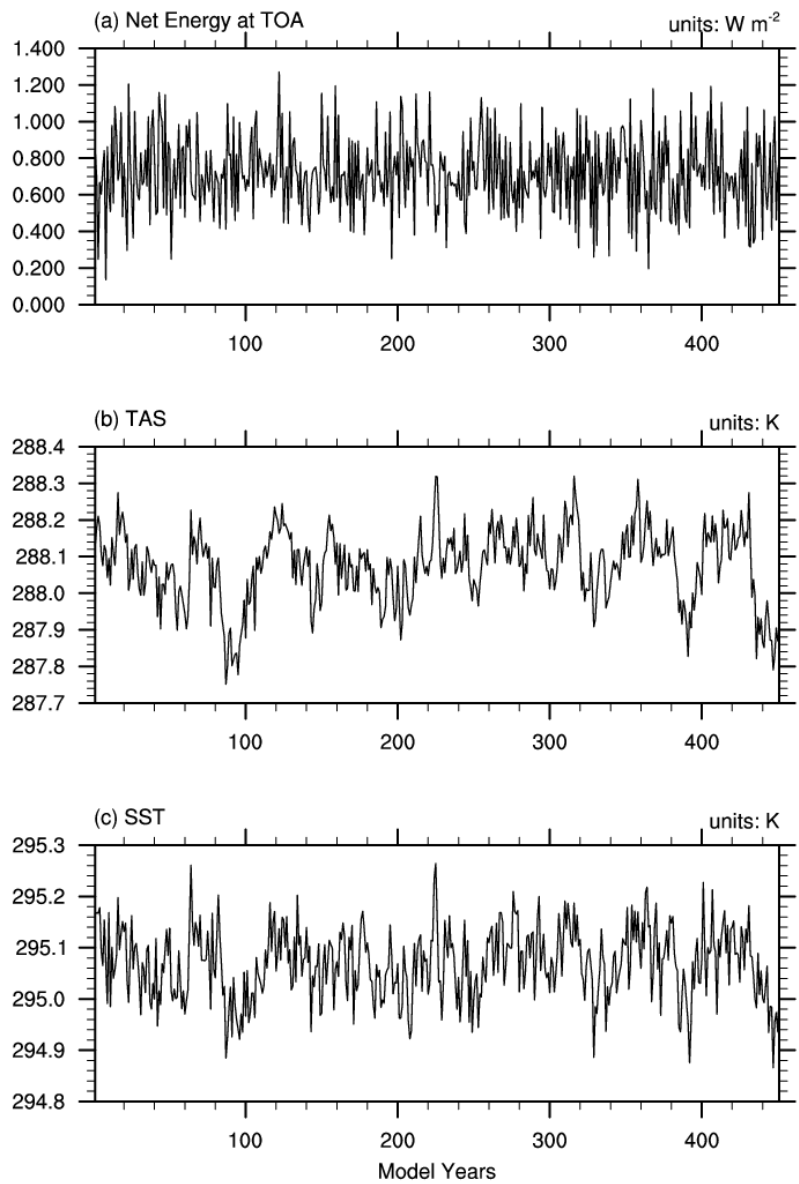


Figure 1. The time series of global and annual mean of (a) net energy budget at top of atmosphere ($W m^{-2}$), (b) near-surface air temperature (K), and (c) sea surface temperature (K) in the last 450 years of the piControl simulation.

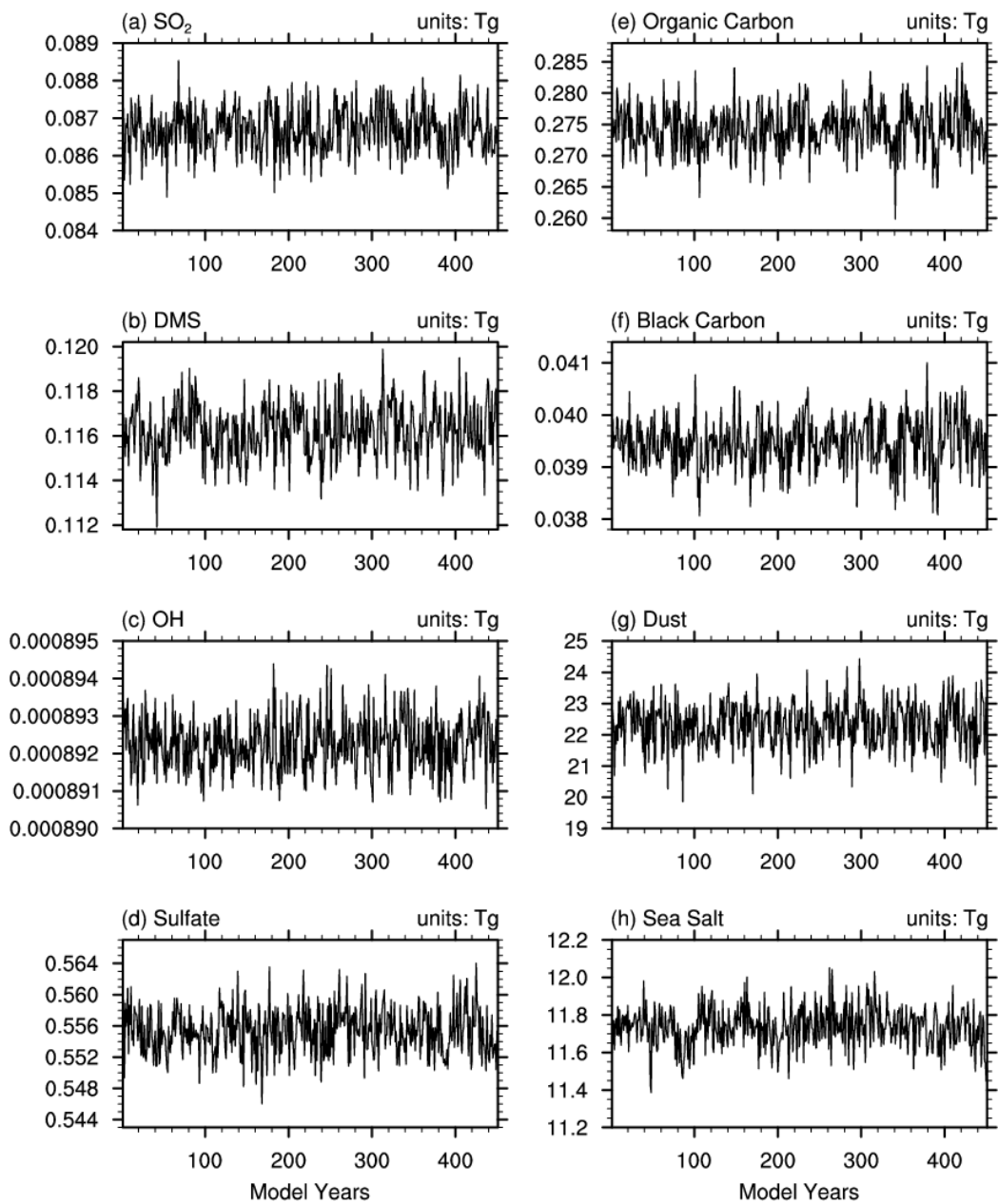


Figure 2. Same as in Figure 1, but for the global burdens of (a) SO_2 , (b) DMS, (c) OH, and (d-h) different aerosols in the troposphere (below 100 hPa). Units are Tg.

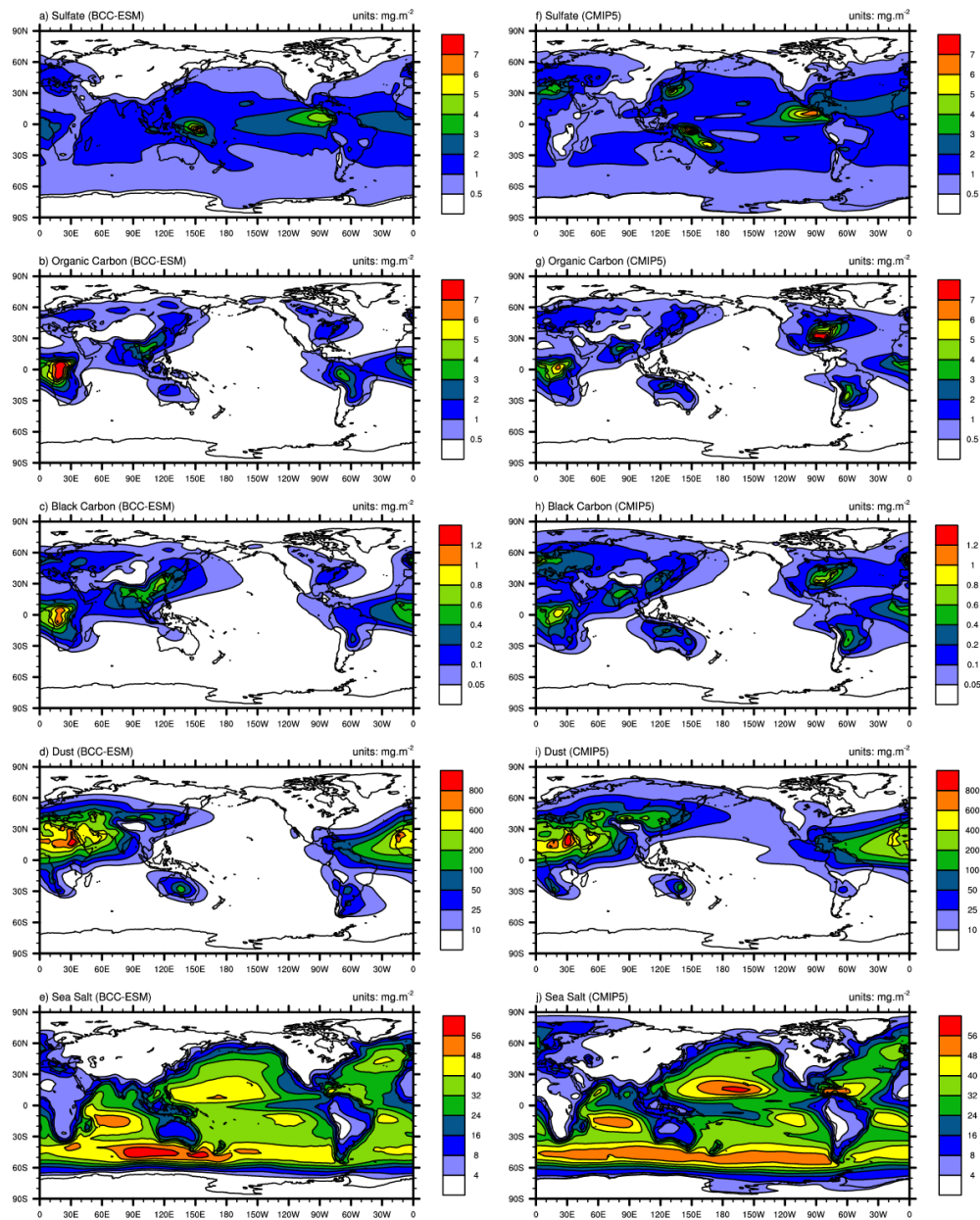


Figure 3. Global distributions of annual mean mass burdens of sulfate (SO_4^{2-} ; first row), organic carbon (OC; second row), black carbon (BC; third row), dust (fourth row), and sea salt (fifth row) aerosols in the whole atmospheric column. The left panels show the mean averaged for the last 100 years of BCC-ESM pre-industrial piControl simulations, and the right panels show the CMIP5 recommended aerosol concentrations in year 1850 (the website at IASA <http://tntcat.iiasa.ac.at/RcpDb/>). Units: mg m^{-2} .

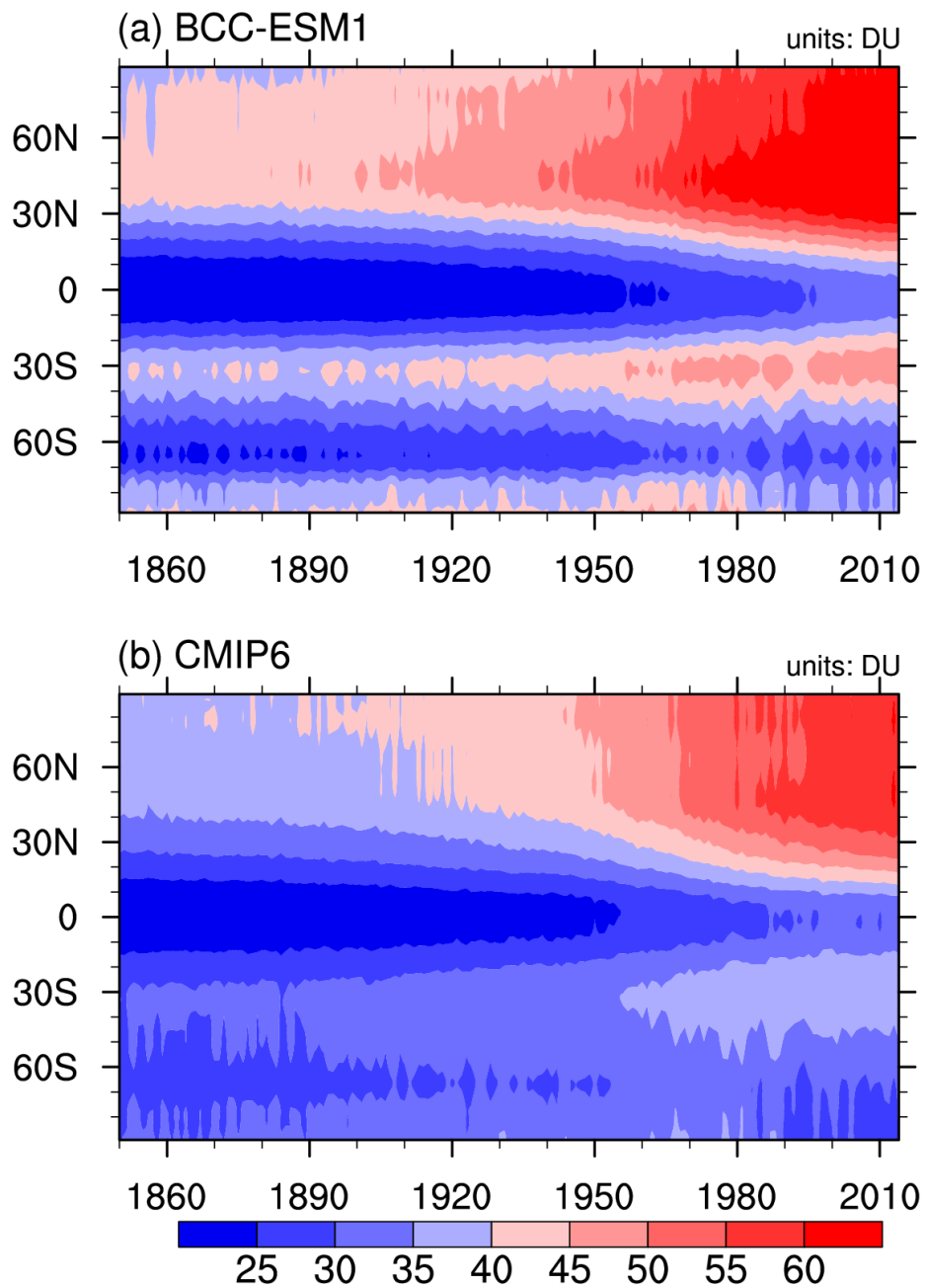


Figure 4. Zonal mean of yearly mean concentration of ozone column in the troposphere below 300 hPa to the ground from 1871 to 1999 for (a) BCC-ESM1 and (b) CMIP6 data. Unit: DU.

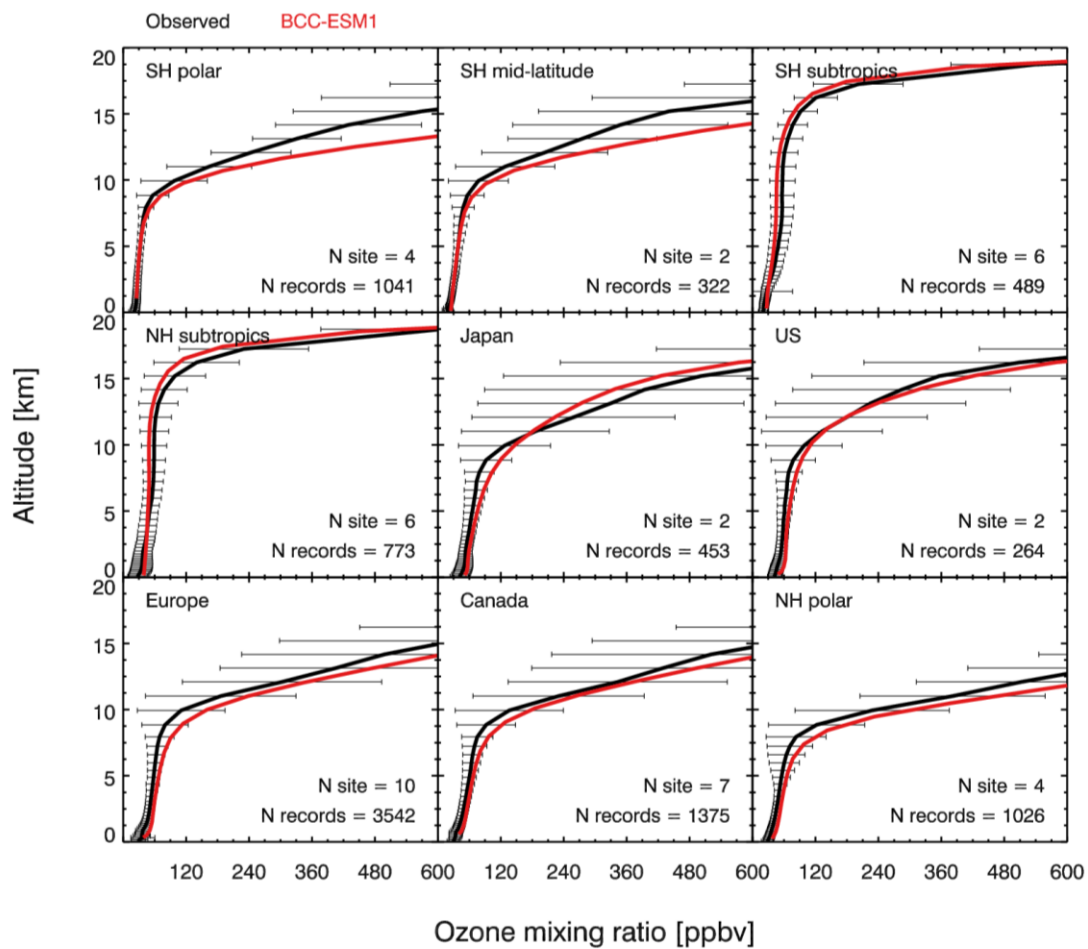


Figure 5. Vertical profiles of annual mean ozone concentrations from observations averaged for 2010-2014 in nine regions (black) and from the BCC-ESM1 simulations (red). The observations are derived from 41 global WOUDC sites.

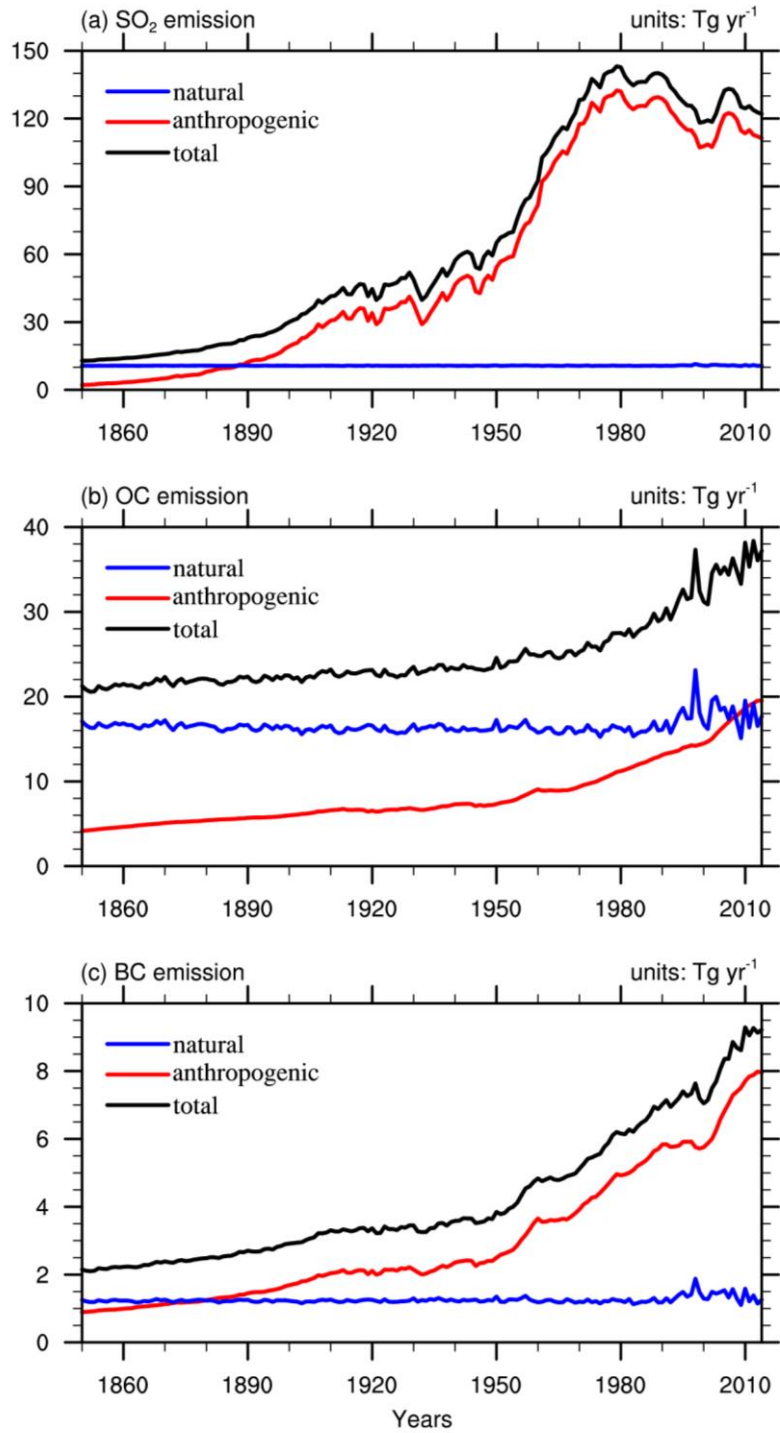


Figure 6. Global annual anthropogenic, natural, and total emissions of SO₂, organic carbon (OC), and black carbon (BC) in the BCC-ESM1 historical simulation. All the biomass burning emissions are included in natural emissions in (a)-(c). Units: Tg yr^{-1} .

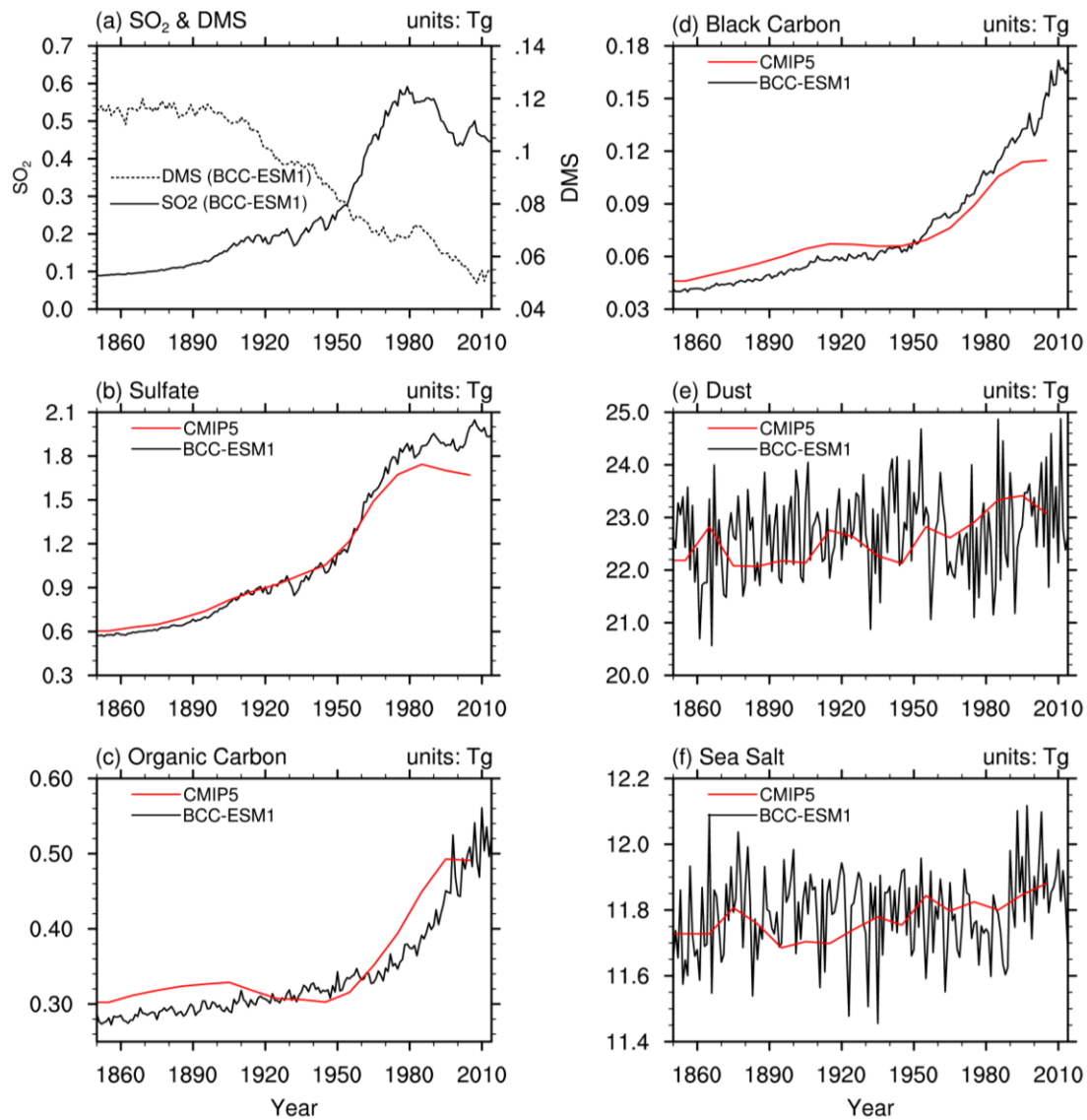


Figure 7. The time series of global yearly amounts of (a) SO₂ and DMS and (b-f) aerosols in the whole atmosphere column from the CMIP6 historical simulations of BCC-ESM1 (black lines) and the CMIP5-recommended aerosols masses (red lines). The yearly CMIP5 data are interpolated from the time series in 10-year interval. Units: Tg.

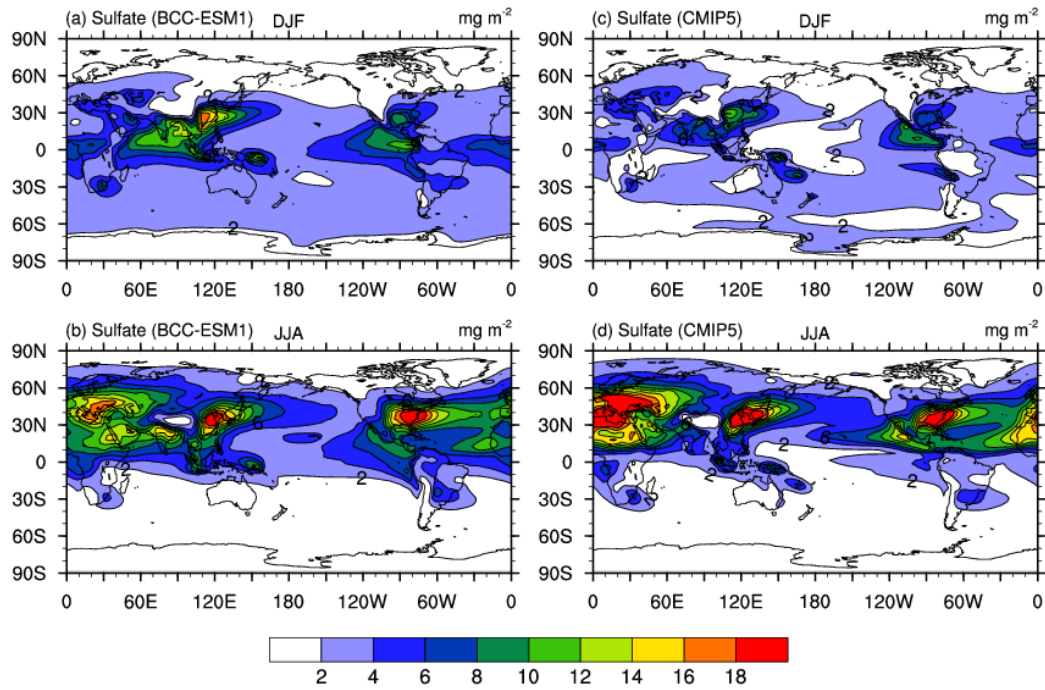


Figure 8. December-January-February (DJF; top panels) and June-July-August (JJA; bottom panels) mean sulfate (SO_4^{2-}) aerosol column mass concentrations averaged for the period of 1971-2000. Left panels show the historical simulations of BCC-ESM1, and right panels the CMIP5-recommended data. Units: mg.m^{-2} .

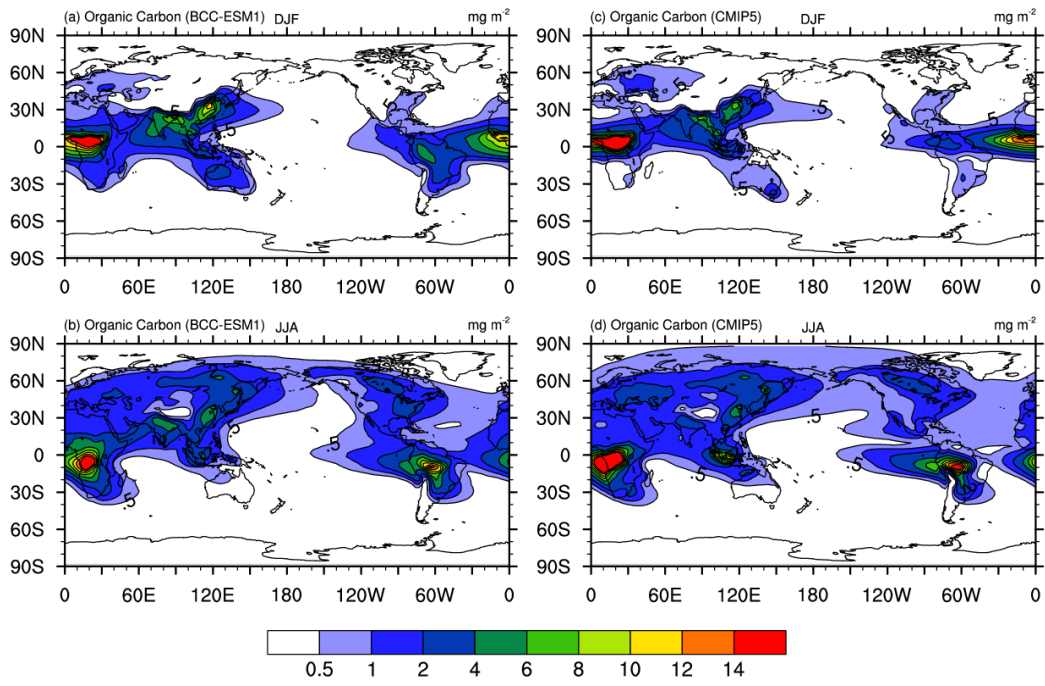


Figure 9. The same as in Figure 8, but for organic carbon (OC) aerosol column mass concentrations. Units: mg m^{-2} .

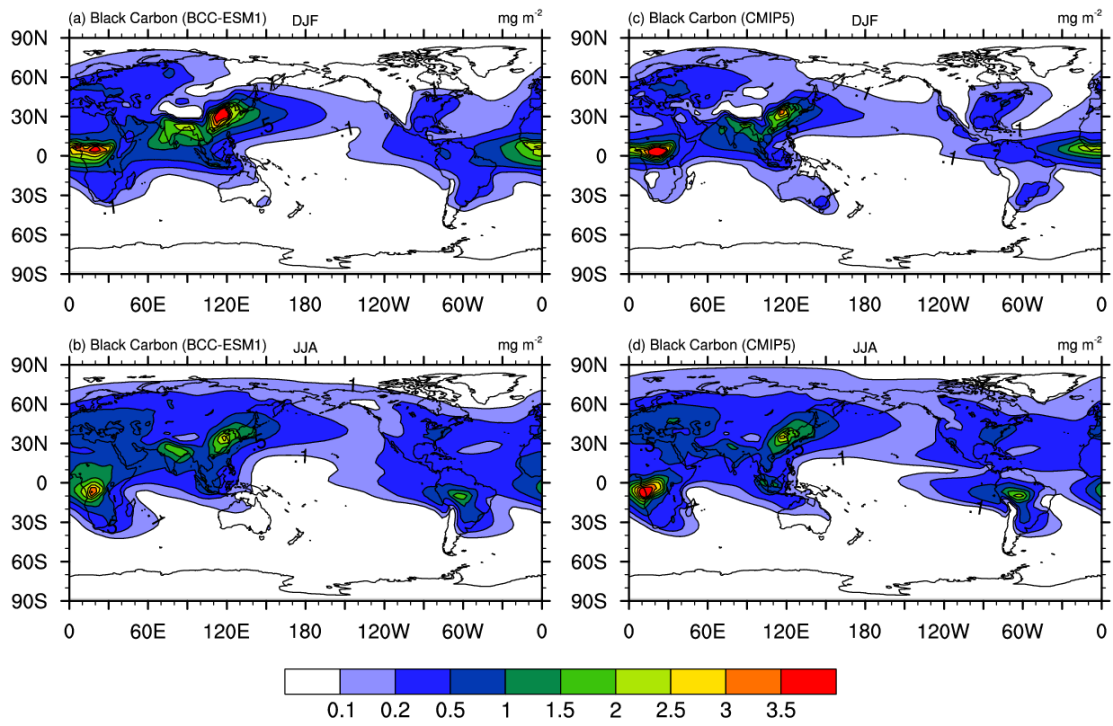


Figure 10. The same as in Figure 8, but for black carbon (BC) aerosol. Units: mg.m^{-2} .

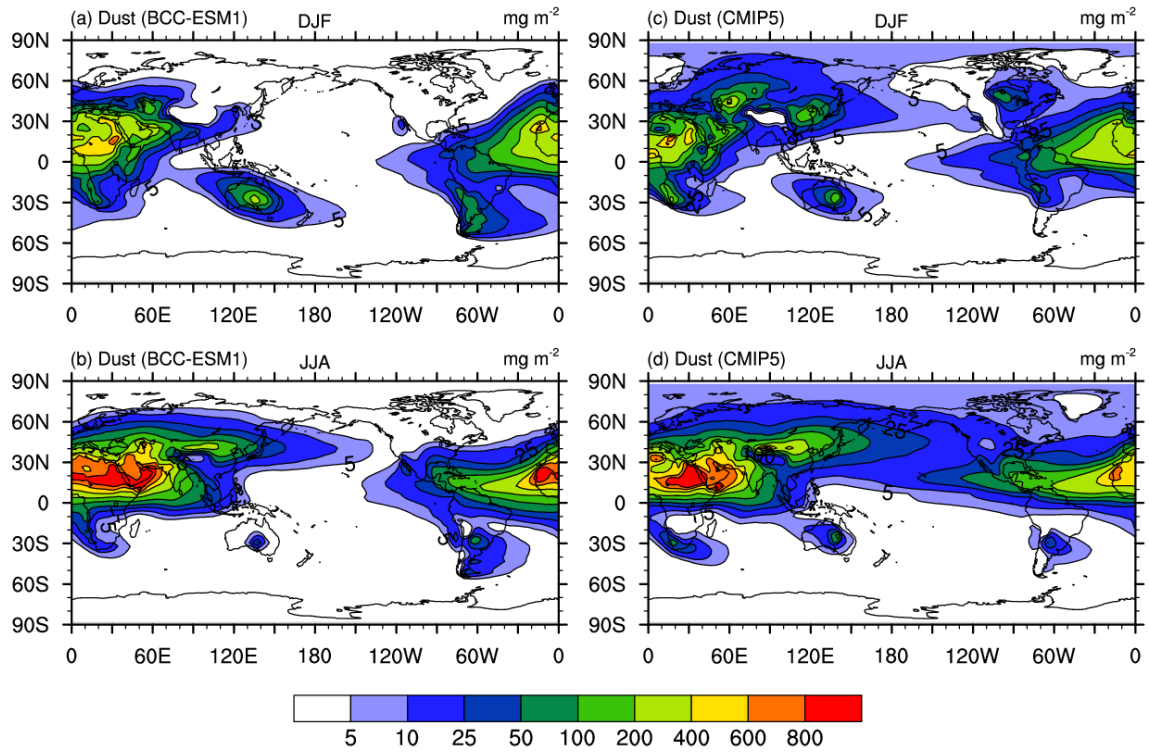


Figure 11. The same as in Figure 8, but for dust aerosol. Units: mg.m^{-2} .

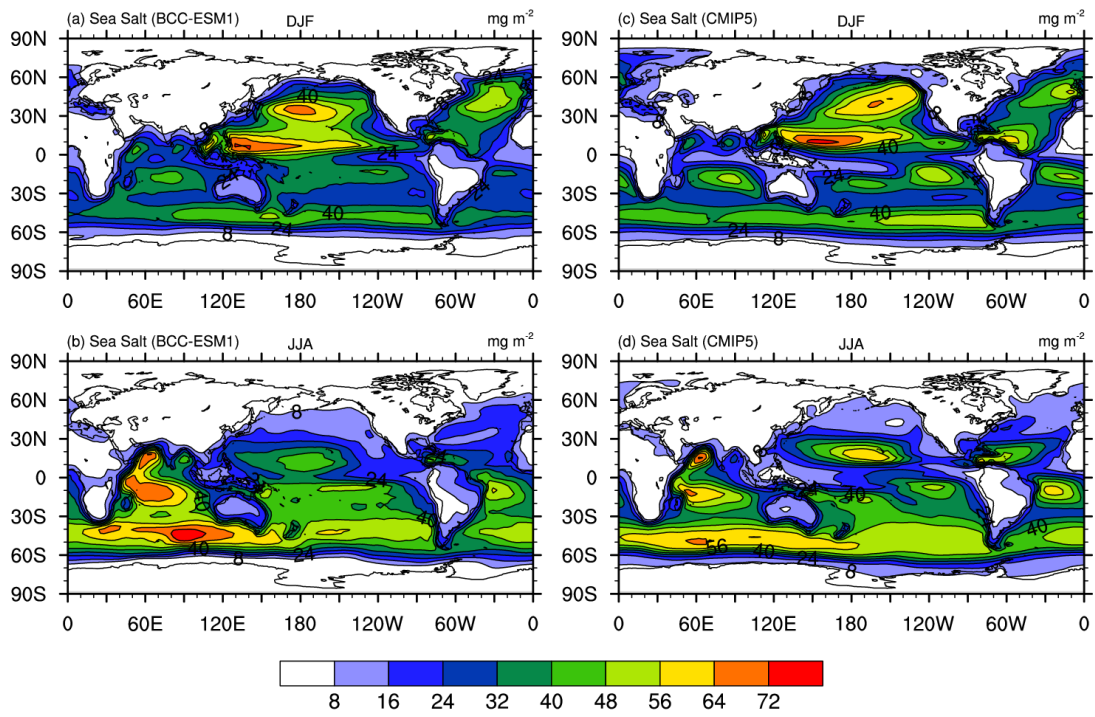


Figure 12. The same as in Figure 8, but for sea salt (SSLT) aerosol. Units: mg.m^{-2} .

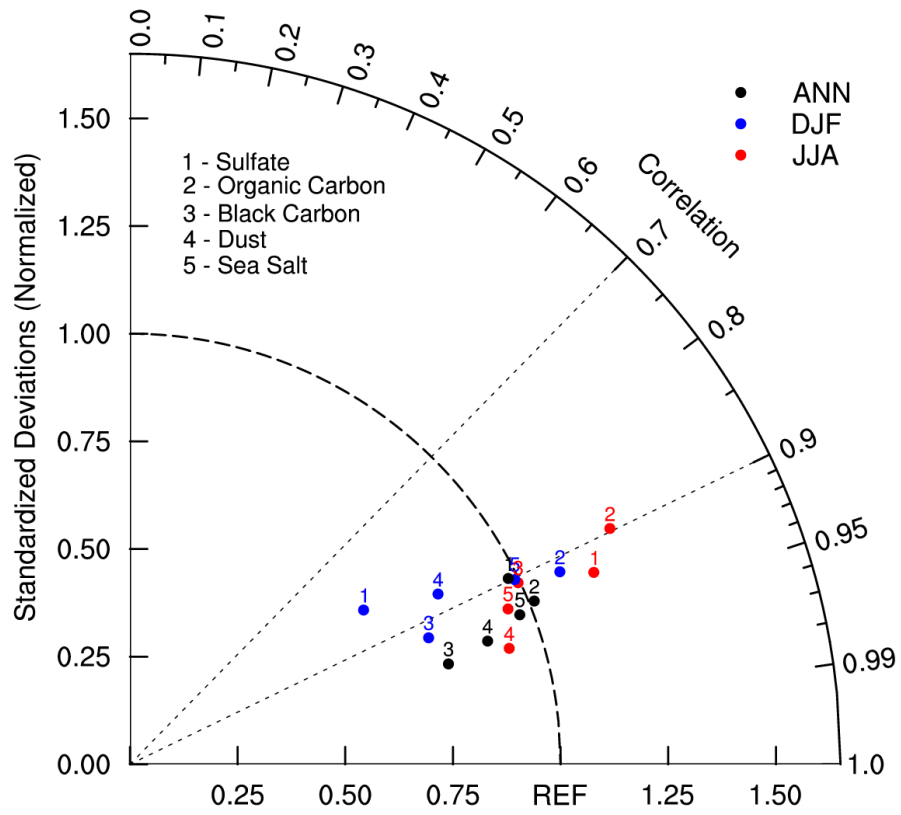


Figure 13. Taylor diagram for the global aerosols climatology (1971–2000) of sulfate, organic carbon, black carbon, dust, and sea salt averaged for December-January-February (DJF), June-July-August (JJA), and annual respectively. The radial coordinate shows the standard deviation of the spatial pattern, normalized by the observed standard deviation. The azimuthal variable shows the correlation of the modelled spatial pattern with the observed spatial pattern. Analysis is for the whole globe. The reference dataset is CMIP5-prescribed dataset.

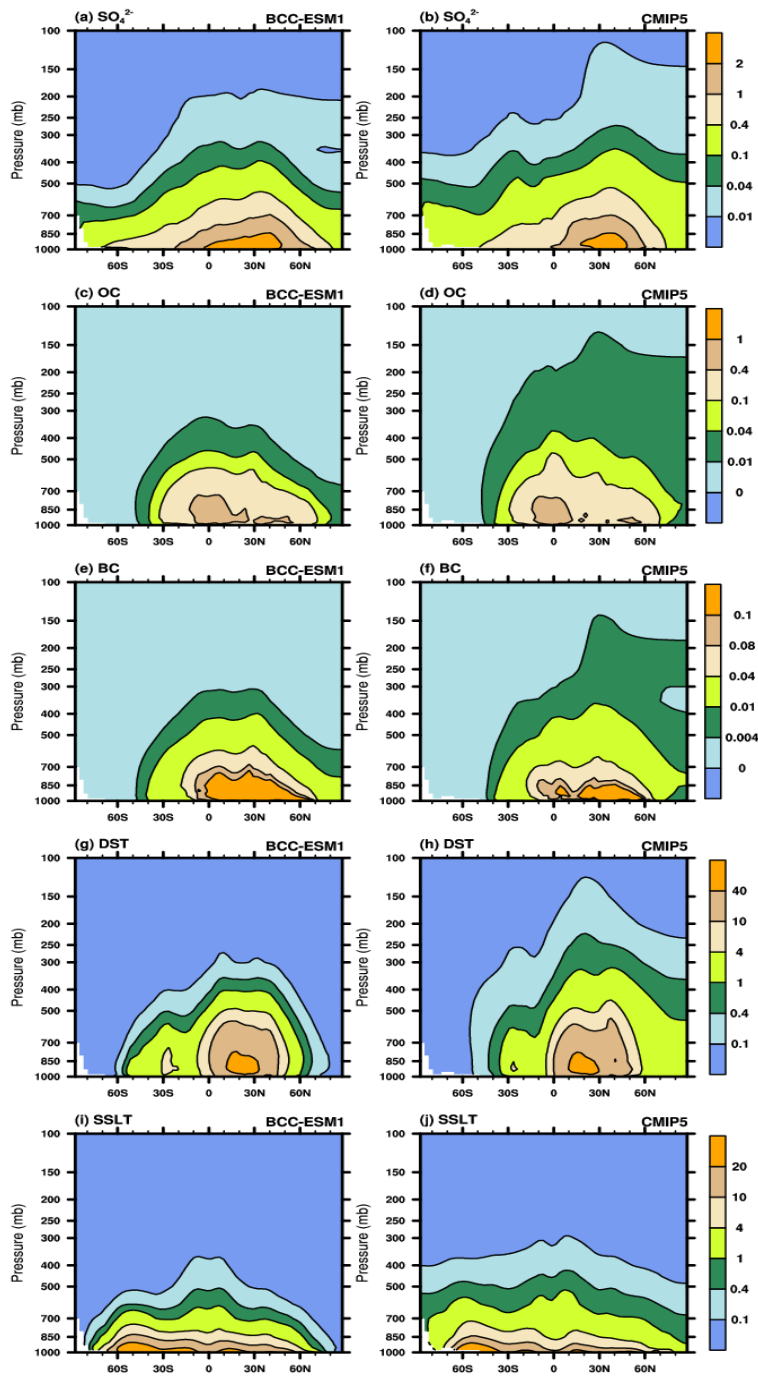


Figure 14. Latitude-pressure distributions of zonally-averaged annual mean sulfate, organic carbon, black carbon, dust, and sea salt aerosol concentrations for the period of 1971-2000. Left panels show the CMIP6 historical simulation of BCC-ESM1, and right panels the CMIP5 recommendation data. Units: $\mu\text{g m}^{-3}$.

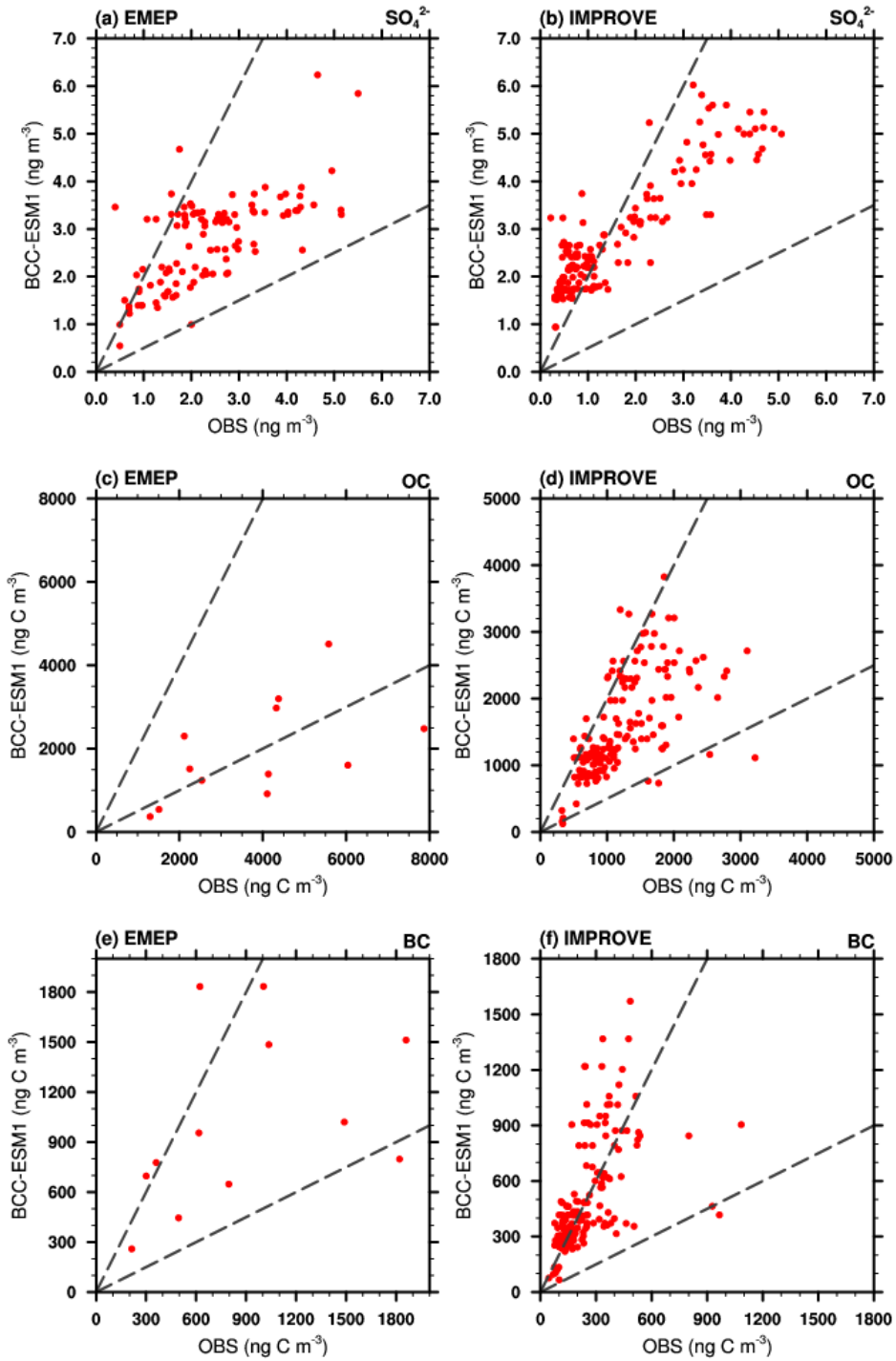


Figure 15. Scatter plots showing observed versus simulated multi-years averaged annual mean sulfate (SO_4^{2-}), organic carbon (OC), black carbon (BC) mixing ratios at IMPROVE and EMEP network sites. Observations are averages over the available years 1990–2005 for IMPROVE sites, and 1995–2005 for EMEP sites. Simulated values are those at the lowest layer of BCC-ESM1.

Table 7. Observed versus simulated concentrations of sulfate (SO_4^{2-}), organic carbon (OC), black carbon (BC) for the regional mean and spatial standard deviation, minimum and maximum values at [HIPPO aircraft observations \(BC only\)](#), IMPROVE and EMEP network sites, and the spatial correlation between observed and simulated multi-years averaged annual means. Simulated values are selected for the same locations and same valid observation time. The data used same as those in Figure 12.

	EMEP			IMPROVE			HIPPO
	SO_4^{2-} (Obs/Model)	OC (OBS/Model)	BC (OBS/Model)	SO_4^{2-} (OBS/Model)	OC (OBS/Model)	BC (OBS/Model)	BC (OBS/Model)
Mean Values	2.37/2.74	3844/1919	884/1022	1.53/2.79	1215/1565	249/504	8.2/11.1
Std Deviation	1.16/0.93	1997/1215	572/526	1.30/1.20	572/745	164/296	27.9/21.0
Min Values	0.40/0.55	1296/369	214/259	0.22/0.94	322/123	45/66	0.0025/0.066
Max Values	5.50/6.24	7867/4510	1859/1834	5.07/6.02	3219/3827	1084/1570	558.91/267.11
Correlation (Obs and Model)	0.67	0.56	0.40	0.90	0.63	0.55	0.51

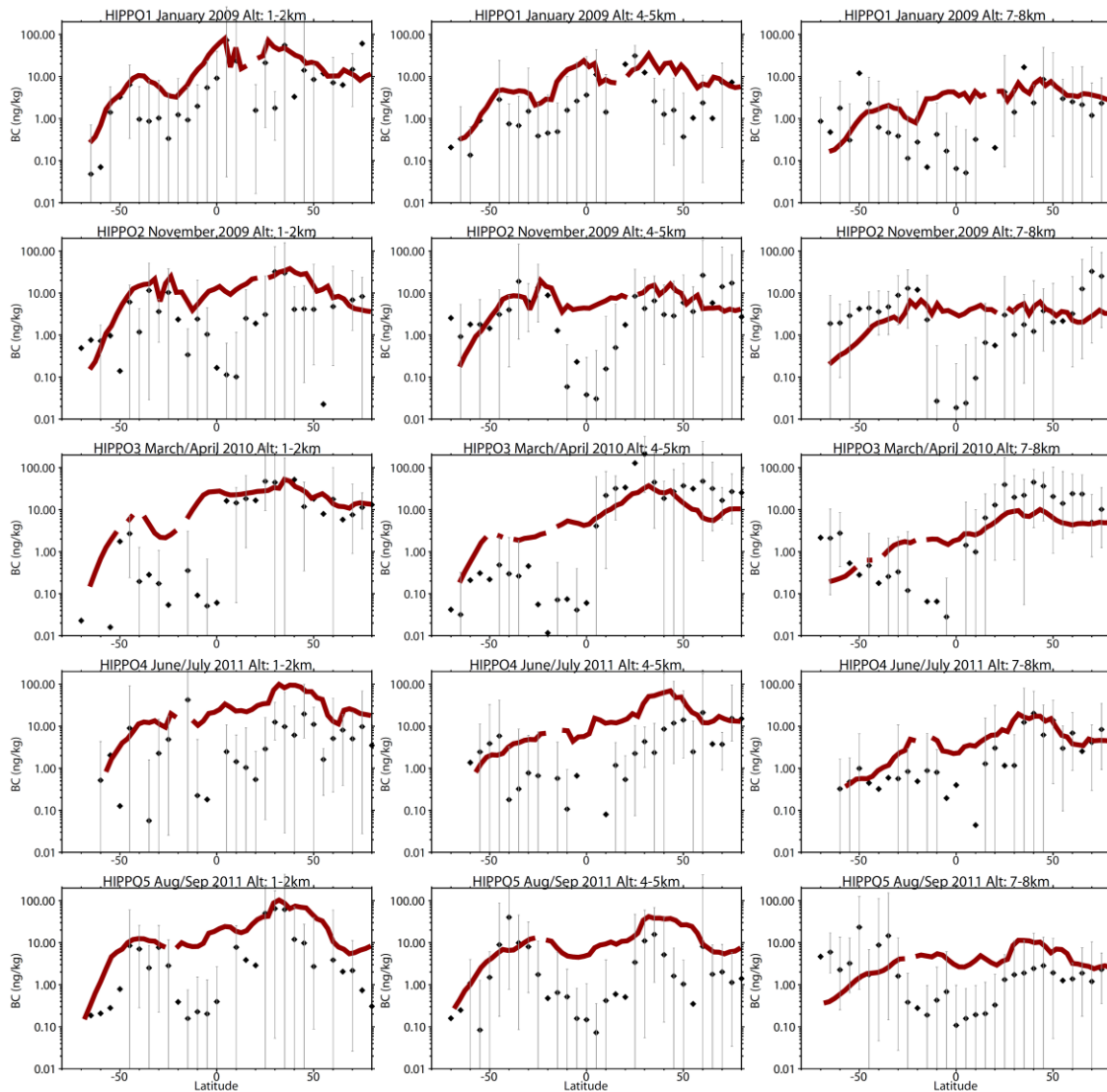


Figure 16. Comparison of modelled black carbon (BC) aerosol (red lines) with observations from HIPPO aircraft campaigns over the Pacific Ocean (black symbols, bars represent the full data range). Observations from different HIPPO campaigns were averaged over 5 °latitude bins and three different altitude bands (left column: 1-2 km, middle column: 4-5 km, and right column: 7-8 km) along the flight track over the Pacific Ocean. Model results were sampled along the flight track and then averaged over the abovementioned regions for comparison.

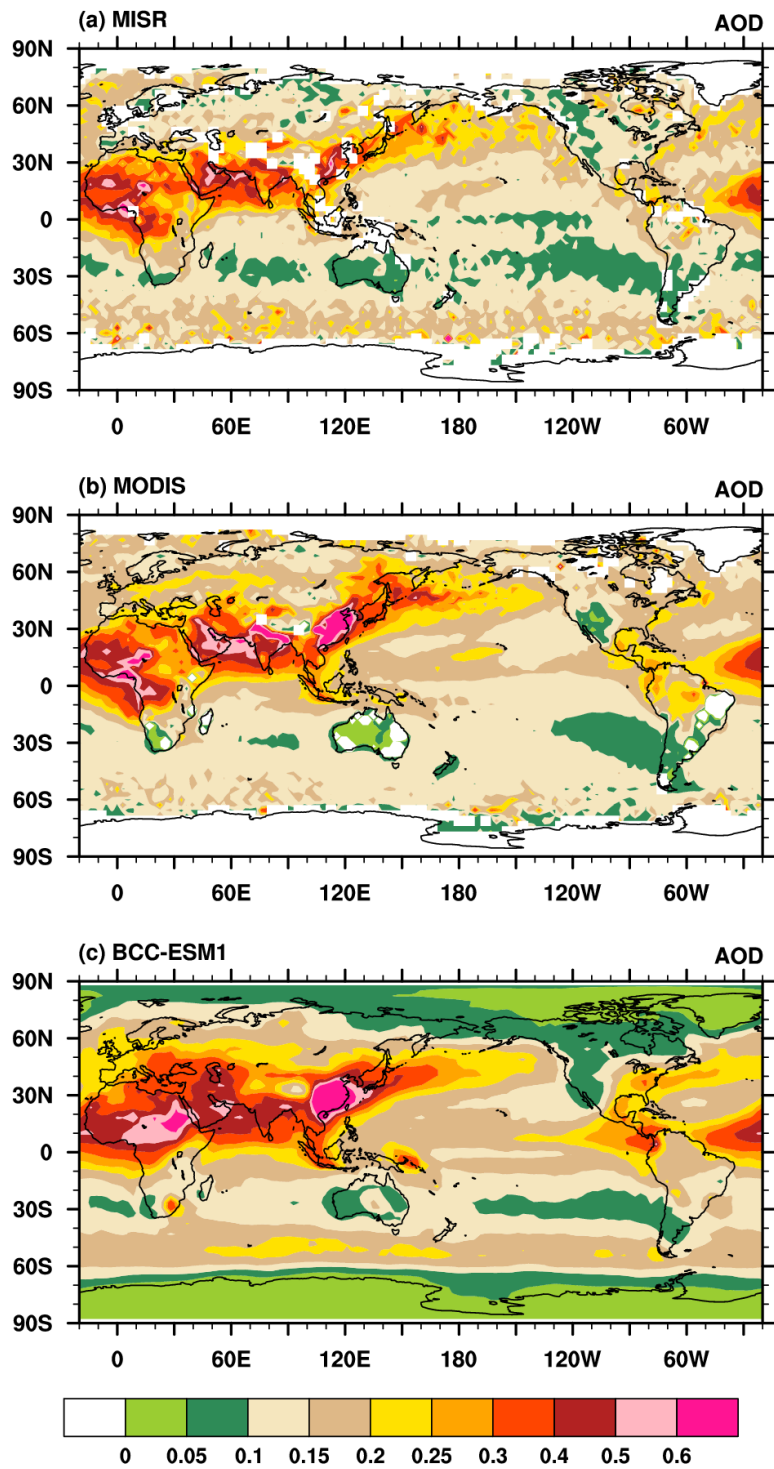


Figure 17. Global distribution of annual mean AOD simulated in BCC-ESM1 compared with the MISR and MODIS data for the year 2008.

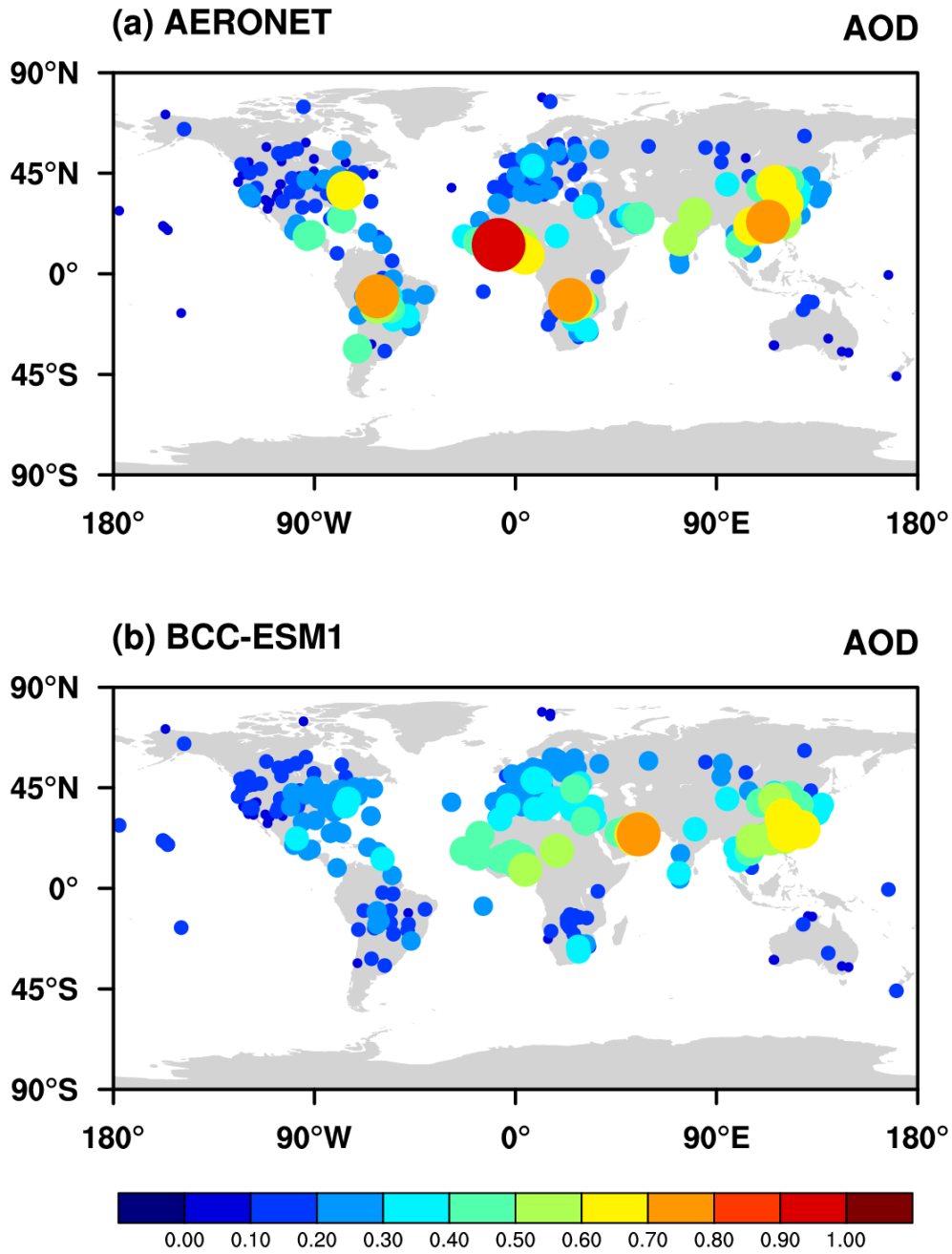


Figure 18. Observed versus simulated annual means of AOD at AERONET sites. Each data point represents the mean averaged for available monthly values of AOD. The dot sizes denote the magnitudes of AOD at sites. The spatial correlation is 0.56.

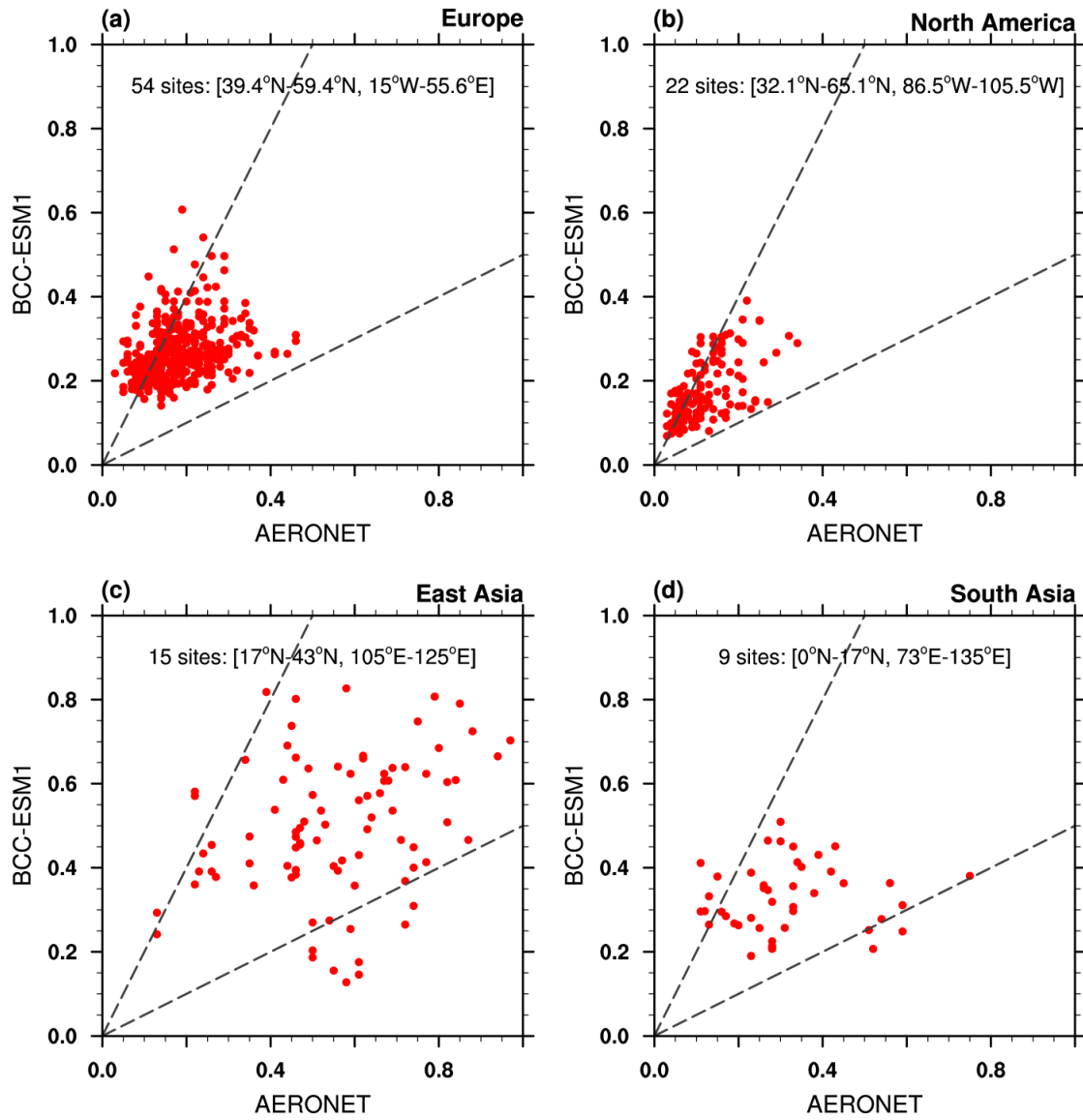


Figure 19. Scatter plots of observed versus simulated monthly mean AOD at AERONET sites in Europe, North America, East Asia, and South Asia over the period of 1998-2005.